Kinematic Structure and Dynamics of the Denmark Strait Overflow from Ship-based Observations

Peigen Lin[1], Robert S. Pickart[1], Kerstin Jochumsen[2], G.W.K. Moore[3], Héðinn Valdimarsson[4], Tim Fristedt[5], Lawrence J. Pratt[1]

1. Woods Hole Oceanographic Institution, Woods Hole, USA

2. Federal Maritime and Hydrographic Agency (BSH), Hamburg, Germany

3. Department of Physics, University of Toronto, Toronto, Canada

4. Marine and Freshwater Research Institute, Reykjavik, Iceland

5. Department of Marine Technology, Multiconsult Norway AS, Tromsø, Norway

May 2020

Submitted to *Journal of Physical Oceanography*

Corresponding author: Peigen Lin (plinwhoi@gmail.com)

Abstract

The dense outflow through Denmark Strait is the largest contributor to the lower limb of the Atlantic Meridional Overturning Circulation, yet a description of the full velocity field across the strait remains incomplete. Here we analyze a set of 22 shipboard hydrographic/velocity sections occupied along the Látrabjarg transect at the Denmark Strait sill, obtained over the time period 1993–2018. The sections provide the first complete view of the kinematic components at the sill: the shelfbreak East Greenland Current (EGC), the combined flow of the separated EGC and the North Icelandic Jet (NIJ), and the northward flowing North Icelandic Irminger Current (NIIC). The total mean transport of overflow water is 3.54 ± 0.29 Sv, comparable to previous estimates. The dense overflow is partitioned in terms of water mass constituents and flow components. The mean transports of the two types of overflow water – Atlantic-origin Overflow Water and Arctic-origin Overflow Water – are comparable in Denmark Strait, while the merged NIJ/separated EGC transports 55% more water than the shelfbreak EGC. A significant degree of water mass exchange takes place between the branches as they converge in Denmark Strait. There are two dominant time-varying configurations of the flow that are characterized as a cyclonic state and a non-cyclonic state. These appear to be wind-driven. A potential vorticity analysis indicates that the flow through Denmark Strait is subject to symmetric instability. This occurs at the top of the overflow layer, implying that the mixing/entrainment process that modifies the overflow water begins at the sill.

1. Introduction

The dense water formed in the Nordic Seas is the main source of lower North Atlantic Deep Water that plays an essential role in the Atlantic Meridional Overturning Circulation (AMOC) (Dickson and Brown, 1994). Studies have now demonstrated that the dominant contribution to the AMOC is associated with the warm-to-cold transformation that occurs in the Nordics Seas as opposed to that which takes place in the Labrador Sea (Pickart and Spall, 2007; Holte and Straneo, 2017; Lozier et al., 2019). Denmark Strait is one of the key passages through which the dense water from the Nordic domain enters the North Atlantic Ocean. The so-called Denmark Strait Overflow Water (DSOW) accounts for roughly half of the total dense water flowing over the Greenland-Scotland Ridge. The mean transport of DSOW at the sill, which is typically defined as water denser than 27.8 kg m^{-3}, is estimated to be 3.2–3.5 Sv (Harden et al., 2016; Jochumsen et al., 2017).

There are three different pathways that advect the dense water into Denmark Strait from the north, supplying the overflow water (Fig. 1): the shelfbreak East Greenland Current (EGC); the separated EGC; and the North Icelandic Jet (NIJ). The EGC emanates from Fram Strait and is a surface-intensified flow transporting Atlantic-origin Overflow Water at depth. At these latitudes it is comprised of a shelfbreak branch and an offshore slope branch (Håvik et al., 2017a). Together they advect a combination of warm, salty water that has been modified along the rim current system of the Nordic Seas (Mauritzen, 1996) and also in the high Arctic (Rudels et al., 2005). The shelfbreak EGC transport decreases as it progresses southward, while the slope branch appears to be diverted eastward into the interior north of the Iceland Sea (Håvik et al., 2017a). When the shelfbreak EGC reaches the northern end of the Blosseville Basin it bifurcates to form the separated EGC (Fig. 1). Våge et al. (2013) attribute the bifurcation to local wind stress curl and topography, as well as baroclinic instability of the shelfbreak current.

The NIJ is a middepth-intensified current on the north Iceland slope that transports Arctic-origin Overflow Water equatorward. This water is colder, fresher, and denser than the Atlantic-origin Overflow Water. It was hypothesized by Våge et al. (2011) that the NIJ is part of a local overturning loop in the Iceland Sea whereby the subtropical-origin water transported northward by the North Icelandic Irminger Current (NIIC, Fig. 1) is fluxed into the interior of the basin and converted to overflow water by wintertime air-sea heat loss. The dense water then progresses back to the Iceland slope where it sinks and feeds the NIJ. However, it has since been demonstrated that the bulk of the Arctic-origin water must originate from farther north where the wintertime mixed layers are denser (Våge et al., 2015). Recent analysis of the historical data suggests that the water stems from the Greenland Sea (Huang et al., submitted). Based on a large collection of shipboard transects occupied over 15 years, Semper et al. (2019) documented that the NIJ steadily increases in transport as it flows towards Denmark Strait, accounting for a sizable fraction of the dense water that overflows the sill.

Using data from a year-long mooring array across the Blosseville Basin (roughly 200 km north of the sill), Harden et al. (2016) calculated mean transports for the three individual pathways: 1.50 ± 0.16 Sv for the shelfbreak EGC, 1.04 ± 0.15 Sv for the separated EGC, and 1.00 ± 0.17 Sv for the NIJ. There was very little seasonal variation, in line with the weak seasonality observed at the sill (Jochumsen et al., 2012). However, Harden et al. (2016) revealed that the transports of the three branches vary on intra-seasonal timescales, and that they tend to compensate each other such that the total overflow transport remains fairly steady. This is suggestive of hydraulic control, which is argued to be active in Denmark Strait (Whitehead, 1989; Nikolopoulos et al., 2003). Harden et al. (2016) argued that wind stress curl forcing causes the compensation between the NIJ and the two EGC branches.

On synoptic timescales, the flow of DSOW is highly energetic (Smith, 1976; Bruce, 1995; Rudels et al., 1999; Girton and Sanford, 2003; Käse et al., 2003; von Appen et al., 2017). Using the mooring data from the afore-mentioned Blosseville Basin array, Huang et al. (2019) demonstrated that high-frequency variability is driven by mean-to-eddy baroclinic conversion at the shoreward edge of the NIJ. Using a year-long mooring array in Denmark Strait, Moritz et al. (2019) resolved the passage of eddies, finding more anticyclones in the deepest part of the strait and more cyclones west of this. Satellite altimetry data have revealed enhanced levels of surface eddy kinetic energy in the vicinity of the strait (Høyer and Quadfasel, 2001; Håvik et al., 2017b).

A series of recent papers have further characterized the high-frequency variability of the DSOW at the sill. Two dominant features have been identified, referred to as boluses and pulses. The former corresponds to the passage of a large lens of overflow water and is associated with cyclonic circulation (von Appen et al., 2017). Mastropole et al. (2017) identified boluses in 46 out of 111 transects across the strait occupied since 1990. These features export the very densest DSOW. Pulses correspond to a thinning and acceleration of the DSOW layer, and are associated with anti-cyclonic circulation (von Appen et al., 2017). The two types of features have been identified in a high-resolution numerical model, with characteristics similar to the observations (Almansi et al., 2017). Both the boluses and pulses result in increased transport of DSOW over a period of several days (von Appen et al., 2017). Almansi et al. (2020) have shown that the surges in transport result in the generation of cyclones downstream of the sill. These are the well-known "DSOW cyclones" that emanate from the strait and propagate southward along the East Greenland continental slope (Bruce, 1995; Spall and Price, 1998; von Appen et al., 2017).

The numerical study of Spall et al. (2019) determined that boluses and pulses are part of a single dynamical process, associated with baroclinic instability of the hydrographic front in Denmark Strait. This front divides the southward-flowing water emanating from the Nordic Seas and the northward-flowing NIIC. The instability process results in frontal meanders that propagate southwestward through the strait. Meander troughs are associated with boluses, whereby the NIIC shifts towards Iceland and more overflow water is present in the center of the strait. Meander crests are associated with pulses, when the NIIC moves farther into the strait towards Greenland. Spall et al. (2019) demonstrated that this process is dictated by the interplay between the confluent mean flow in the strait that tends to sharpen the front, and the baroclinic instability which works to relax the front. These results show that the dynamics of the DSOW are closely tied to those of the NIIC.

Based on the large number of shipboard occupations of the Látrabjarg transect across Denmark Strait (Fig. 1), we now have a good characterization of the two-dimensional hydrographic structure across the strait. However, we lack an analogous view of the kinematic structure. Over the years, moorings have been deployed in the deepest part of the sill, which is referred to as the trough (see Fig. 4). These timeseries have provided information on the vertical structure and transport of the overflow water (e.g. Jochumsen et al., 2017; von Appen et al., 2017; Spall et al., 2019). Recently a five-mooring array was deployed on the western flank of the trough. Using empirical orthogonal function analysis on the velocity timeseries, Jochumsen et al. (2017) found that the first mode reflects a barotropic flow that pulses in time, the second mode represents lateral shifts of the flow, and the third mode corresponds to the mesoscale eddy features noted above, investigated by Moritz et al. (2019). While these measurements have enhanced our understanding of the flow components in Denmark Strait, they are limited in cross-strait coverage and only have near-bottom temperature and salinity information.

In this study we analyze the updated collection of shipboard occupations of the Látrabjarg line (Fig. 1). The number of occupations is now 122, and, importantly, 22 of them contain direct velocity measurements. This provides the first-ever robust view of the two-dimensional velocity structure across the strait. It enables us to determine the fate of the three above-mentioned pathways of overflow water into Denmark Strait, including the water masses they advect and their relationship to the NIIC. We are also able to investigate dynamical aspects of the overflow. The paper is organized as follows. We begin with a presentation of the data. This is followed by a description of the mean hydrographic and velocity structure and the partitioning of the overflow transport by water masses and currents. We then characterize the dominant mode of variability and its relationship to local wind forcing. Finally, we address the hydraulic criticality of the overflow, including the occurrence of symmetric instability and implications for mixing.

2. Data and Methods

2.1. Látrabjarg sections

We use 122 occupations of the Látrabjarg hydrographic transect across Denmark Strait taken between 1990 and 2018 (Fig. 2). This is an updated version of the dataset used by Mastropole et al. (2017), who analyzed 111 of the sections (1990–2012; see Table 1 in Mastropole et al., 2017). A detailed description of the conductivity-temperature-depth (CTD) data and the processing steps are described in Mastropole et al. (2017). Briefly, each occupation is projected onto the standard Látrabjarg line (black line in Fig. 2), and gridded vertical sections of the hydrographic variables are constructed. We followed the same procedure for the 11 additional occupations, which are listed in Table 1. Here we also use direct velocity information obtained on 22 of the sections (Table 1; Fig. 3). This consisted of vessel-mounted acoustic Doppler current profiler (ADCP) data (15 of the occupations) and lowered ADCP data (7 of the occupations). Our study focuses primarily on the 22 occupations with velocity data, except for Section 5 where the full historical hydrographic dataset is used.

Absolute geostrophic velocity sections were computed using the gridded hydrographic sections in conjunction with gridded sections of the cross-track ADCP velocities, following the same procedure as in Pickart et al. (2016). Errors in the volume transport estimates are associated with instrument uncertainty, the gridding process, and the inability to measure the flow in the "bottom triangles" (the area beneath the deepest common level of adjacent stations). Because of the generally small station spacing of the sections, the latter effect is taken to be negligible. The uncertainties of both the vessel-mounted ADCP and lowered ADCP are taken as 0.02 m s^{-1} (Pickart et al., 2016, 2017). The gridding error was obtained by calculating the differences between the vertically-averaged velocity measurement at each station versus the same quantity determined using the gridded values closest to the station (Nikolopoulos et al., 2009). The final error is taken to be the root of the sum of the squares of the instrument and gridding errors, and is applied over the area of the section where the transport is being calculated. Since this does not assume that the errors are uncorrelated, it represents a conservative estimate.

2.2. Reanalysis Wind Data

Wind fields from the ERA5 reanalysis were obtained from the European Center for Medium-Range Weather Forecasts (ECMWF, https://www.ecmwf.int/). This is the 5th generation reanalysis, which uses ECMWF's Integrated Forecast System (IFS). Previous studies have shown good agreement between IFS products and observations (Harden et al., 2016). The spatial resolution of ERA5 is 0.25°. Here we used the 3-hourly product from 1990 to 2018.

2.3. Satellite Absolute Dynamic Topography

The along-track absolute dynamic topography (ADT) data used in the study were provided by the Copernicus Marine and Environment Monitoring Service (CMEMS, http://www.marine.copernicus.eu). The product is processed by the Data Unification and Altimeter Combination System (DUACS) which applies to multi-mission altimeter data. The data are comprised from the TOPEX/POSEDON mission, together with the Jason-1, Jason-2, and Jason-3 missions. Since Denmark Strait is close to the northern turning point of the orbits, the along-track data have spatial and temporal resolutions of roughly 12 km and 2 days, respectively. The time period of data coverage used here is 1993 to 2018.

3. Basic Characteristics

3.1. Mean State

We first present the mean Látrabjarg sections of hydrography and absolute geostrophic velocity using the 22 realizations that include velocity data (Fig. 4). We don't consider the regions on the east and west side of the strait where the number of occupations is less than five. Encouragingly, the mean distributions of potential temperature and salinity are consistent with the analogous means presented in Mastropole et al. (2017) using 111 occupations. It indicates that our mean view using a smaller number of sections is representative. The warm and salty water on the Iceland shelf is the Irminger Water originating from the south (the near-surface fresh water at the eastern end of the section is likely associated with the Iceland coastal current, Logemann et al., 2013). To the west, the vertically varying temperature and salinity reflects several water masses. In the upper layer, the cold and fresh water, referred to as Polar Surface Water, emanates from the Arctic Ocean via Fram Strait (de Steur et al., 2009; Håvik et al., 2017a). Beneath this, the warm water at the western edge of the section, centered near 150 m, is Irminger Water that has recirculated north of the strait (Mastropole et al., 2017; Casanova et al., submitted). Near the bottom is the DSOW, denser than 27.8 kg m^{-3} (this isopycnal is highlighted in Fig. 4). As noted above, this is a combination of Atlantic-origin Overflow Water (AtOW) and Arctic-origin Overflow Water (ArOW), which is banked up on the western side of the trough (see also Våge et al., 2011; Harden et al., 2016; Mastropole et al., 2017). The breakdown between these water masses is addressed in the next section.

Figure 4d shows the mean section of absolute geostrophic velocity. This is the first such view of the average, full water column velocity structure across Denmark Strait. The strong poleward flow in the vicinity of the Iceland shelfbreak is the NIIC, which transports Irminger Water into the Iceland Sea. Seaward of the NIIC there are two bands of southward, bottom-intensified flow associated with tilting isopycnals sloping downward from west to east. The stronger band of flow is located on the western side of the deep trough and transports the densest DSOW. The second band is situated near the East Greenland shelfbreak. As noted above, the NIJ, separated EGC, and shelfbreak EGC all advect water into Denmark Strait (Fig. 1). The year-long mooring dataset across the Blosseville Basin used by Harden et al. (2016) revealed that, in the mean, the NIJ and separated EGC were partially merged at that location. Our results demonstrate that, in Denmark Strait, these two currents are fully merged and correspond to the stronger band of flow in Fig. 4d which transports the majority of the DSOW. The weaker band of flow to the west is the shelfbreak EGC. Note, however, that there is only a slight minimum in flow between the shelfbreak EGC and the merged NIJ/separated EGC (Fig. 4d), which indicates that all three branches have combined to some degree in the narrow strait.

3.2. Partitioning the DSOW Transport

The transport of DSOW (denser than 27.8 kg m^{-3}) in the vicinity of Denmark Strait has been estimated in many studies. Harden et al. (2016) reported a year-long mean value of 3.54 ± 0.16 Sv from the mooring array across the Blosseville Basin in 2011–12. Jochumsen et al. (2012) estimated the value to be 3.40 ± 0.60 Sv using one or two moorings in the center of the strait from 1996–2011. This value was later updated by Jochumsen et al. (2017) to be 3.20 ± 0.50 Sv, accounting for known biases in the near-bottom current measurements and using a new method developed from extended measurements. Based on the mean section of Fig. 4d, we obtain a transport of 3.00 ± 0.29 Sv (Table 2). This is lower than the previous estimates because our mean section only extends ~20 km west of the East Greenland shelfbreak. Transects that extend across the entire Denmark Strait reveal that DSOW is found far onto the Greenland shelf, and the limited velocity information there implies weak mean flow (Brearley et al., 2012; Jochumsen et al., 2012). The Greenland shelf contribution in the model of Macrander (2004) is roughly 0.40 Sv, which has been accounted for in the estimates of Jochumsen et al. (2012). Results from a mooring on the Greenland shelf (30 km west of the trough) implied a similar value of 0.50 Sv (Jochumsen et al., 2017) (the mooring array used by Harden et al. (2016) encompassed the DSOW on the Greenland shelf). Linearly extrapolating our mean section of Fig. 4d to the Greenland coast gives a value of 0.54 Sv for the missing transport, which is in line with the estimates above. Thus, our adjusted total transport of 3.54 ± 0.29 Sv is comparable to the previous DSOW transport estimates.

Our hydrographic and velocity data provide the opportunity to partition the overflow transport by water masses. To do this, we applied the same water mass end-member technique of Mastropole et al. (2017) to our 22 occupations. Mastropole et al. (2017) defined four endmembers: AtOW, ArOW, Polar Surface Water, and Irminger Water. They devised two mixing triangles, one of which used the first three water masses, and the other using the latter three water masses – the assumption being that AtOW does not mix with Irminger Water. For each station of a given occupation we computed the corresponding end-member percentages, then gridded these to make vertical sections. The mean sections of percentage for the two types of overflow water are shown in Fig. 5.

The ArOW dominates the deep trough where the merged NIJ/separated EGC is located, accounting for close to 100% of the overflow water near the bottom. By contrast, the AtOW percentage is highest in the vicinity of the Greenland shelfbreak, with large values in the shelfbreak EGC. Note, however, that the percentage of ArOW is comparable to that of the AtOW in this region – this further indicates merging/mixing of the three branches. Using the mean water mass end member percentage sections (Fig. 5) in conjunction with the mean velocity section (Fig. 4d), we get a transport of 1.72 ± 0.15 Sv for ArOW and 0.95 ± 0.10 Sv for AtOW (Table 2). If we assume that the unresolved portion of the flow on the Greenland shelf is predominantly AtOW, this boosts the transport of this water mass to 1.49 ± 0.10 Sv. Hence, we conclude that the mean transports of the two types of overflow water are comparable in Denmark Strait. The remaining transport (0.33 ± 0.04 Sv) corresponds to small contributions from the Polar Surface Water and Irminger Water getting mixed into the top of the overflow layer.

As noted in the introduction, Harden et al. (2016) partitioned the overflow transport into the three flow branches using data from the upstream Blosseville Basin mooring array. Using four shipboard occupations of the same line, Våge et al. (2013) did the same partitioning with generally consistent results. While the two bands of enhanced southward flow in our mean velocity section reflect the shelfbreak EGC and merged NIJ/separated EGC, respectively (Fig. 4d), the degree to which all three branches have merged/mixed in the strait makes it impossible to do precise partitioning here. It is nonetheless instructive to consider the geographical distribution of the overflow transport.

We specify the boundary between the nominal shelfbreak EGC and merged NIJ/separated EGC to be -25 km (i.e. the location of the velocity minimum between the two bands, Fig. 4d). It follows that the shelfbreak EGC transports 0.85 ± 0.14 Sv, while the merged flow accounts for 2.15 ± 0.15 Sv (Table 2). By comparison, Harden et al. (2016) calculated 2.04 ± 0.16 Sv for the merged flow and 1.50 ± 0.16 for the shelfbreak EGC. It is safe to assume that the inshore flow on the Greenland shelf at the Látrabjarg line originated from the shelfbreak EGC upstream (recall that Blosseville mooring array captured all of the overflow water on the Greenland side, which was confined to the region of the shelf edge). This increases our shelfbreak EGC transport to 1.39 ± 0.14 Sv, in line with the Blosseville Basin estimate. Hence, our total transport, as well as the geographical distribution of transport across the strait, is consistent with Harden et al.'s (2016) upstream partitioning. With regard to the overflow water masses, our mean sections (Figs. 4d and 5) indicate that the band of flow at the shelfbreak transports comparable amounts of AtOW and ArOW, while the band of flow on the western flank of the trough transports roughly twice as much ArOW as AtOW (Table 2). Again, this attests to the significant degree of exchange between the flow branches as they converge in Denmark Strait.

4. Dominant Variability

We now consider the section to section variability in our 22 occupations, which is a reflection of mesoscale processes. Using a mooring in the center of the Denmark Strait trough, von Appen et al. (2017) showed that the two pronounced mesoscale features, boluses and pulses, are associated with a cyclonic and anticyclonic sense of rotation, respectively. Following the definitions in

Mastropole et al. (2017), we identified 8 instances of a bolus and 9 instances of a pulse in our collection of sections, (5 sections could not be classified as either type of feature). We found relatively little difference in the across-strait structure of the alongstream velocity field in these two scenarios. However, inspection of the individual sections revealed 15 cases characterized by a strong cyclonic structure centered in the trough. Figure 6 shows the composite mean of these realizations, compared to the composite of the remaining 7 sections (where again we have only plotted regions with at least five realizations). In the former case, which is referred to as the cyclonic state, both the northward-flowing NIIC near the Iceland shelfbreak and the southward-flowing merged NIJ/separated EGC on the western flank of the trough are intensified, while the shelfbreak EGC is weakened. In the latter case, referred to as the non-cyclonic state, the entire trough contains equatorward flow, but it is weaker and more bottom-trapped. In addition, the NIIC is weaker but there is enhanced poleward flow over much of the Iceland shelf. (The data coverage is insufficient to say anything about the shelfbreak EGC in this state.) The hydrographic structure is not noticeably different in the two states (not shown). The height of the overflow layer (i.e. the height of the 27.8 kg m^{-3} isopycnal) is also similar in both composites, although the stronger flow in the cyclonic composite results in a larger transport of DSOW. It is clear that these two states are not reflective of boluses and pulses, which begs the question: what is the nature of this dominant variability? We argue that it is related to wind forcing.

To help demonstrate this, we first characterized the velocity structure in the center of each section by the lateral gradient of the depth-mean velocity across the trough. This is an effective metric that characterizes the degree to which a given section is in the cyclonic state (i.e., the stronger the gradient, the more cyclonic, and vice versa). Using the ERA5 reanalysis wind data, we then created composites of the wind stress curl and wind vectors for the two extremes of the velocity gradient, in particular the five strongest cases and five weakest cases (Fig. 7). The mean wind field during the time of occupation the sections (see Table 1) go into the composites. In the former, the wind in Denmark Strait is strongly out of the northeast and there is pronounced negative wind stress curl over the Blosseville Basin. In the other extreme, the wind is weak and variable, while the wind stress curl is weakly positive over the Blosseville Basin. Våge et al. (2013) showed that negative wind stress curl, together with the closed isobaths of the Blosseville Basin, plays an important role in the bifurcation of the EGC at the northern edge of the basin. This in turn would weaken the shelfbreak EGC. Hence, the wind stress curl pattern in Fig. 7a is conducive for enhancement of the merged NIJ/separated EGC in the trough and decreased flow of the shelfbreak EGC, as seen in the composite of Fig. 6a. In the other extreme the wind stress curl would weaken the merged flow, consistent with the composite of Fig. 6b.

The wind stress curl forcing, however, does not explain the variation in the NIIC between the two states. To address the potential role of the along-strait wind, we employed the along-track ADT data (Figure 2 shows the satellite tracks in the region). Using the 25 years of ADT data, we computed the cross-track component of surface geostrophic velocity for each of the satellite crossings and projected these to the Látrabjarg line (see Spall et al. (2019) for details on the methodology). We note that both the NIIC and merged NIJ/separated EGC have a strong surface signature (Fig. 4). Next, we created composites of the surface velocity corresponding to the associated wind conditions in the strait (averaged in a 1°×1° box around the trough). In particular, we composited all of the satellite crossings for strong northeasterly wind (greater than the mean plus one standard deviation), strong southwesterly wind (same criterion), and for all remaining cases. The results are shown in Figure 8. This demonstrates that when the winds are strongly out of the northeast the NIIC is both stronger and located more seaward, plus the merged NIJ/separated

EGC is enhanced as well. This is consistent with the fact that the cyclonic state (Fig. 6a) corresponds to strong northeasterly winds (Fig. 7a).

We note that in Fig. 8c that the signatures of the NIIC and merged NIJ/separated EGC are much broader than in the cyclonic velocity composite, plus the NIIC is located on the Iceland shelf and the merged flow is located near the Greenland shelfbreak, versus being situated close to the trough. This is likely due in part to the resolution of the altimeter (12 km) which is not well suited for resolving either flow, plus the compositing process. However, it is also partly due to the fact that not all instances with strong northeasterly wind correspond to a strong NIIC displaced to the west – although this is clearly the case in the mean (Fig. 8c). To assess this, we composited the surface geostrophic velocity for all of the instances when the NIIC was at the edge of the Iceland shelf, regardless of wind conditions. This revealed a significantly narrower, stronger NIIC along with an enhanced southward-flowing merged NIJ/separated EGC. Importantly, the mean wind for these instances was strongly out of the northeast. This, together with Fig. 8c, indicates that the cyclonic state in Denmark Strait is clearly associated with enhanced northeasterly winds through the strait.

It remains to be determined what the physical mechanism is behind this change in the NIIC. Upwelling-favorable northeasterly winds should drive southward flow on the Iceland shelf due to Ekman set up, i.e. the opposite of an enhanced NIIC, but the altimeter data are too inaccurate near the coast to confirm this. The strong cyclonic flow offshore, in the vicinity of the trough, is associated with a depression of the sea surface height. Such a signature would arise if there was an increase in wind speed near the center of the strait, due to divergence of the offshore Ekman transport. Unfortunately, the spatial resolution of ERA5 (~30 km) is insufficient to resolve such a change. It should be noted that a two-dimensional view may not be appropriate here because the presence of warm, relatively light water along the south coast of Iceland and cold, dense water along the north slope, will result in an anti-cyclonic propagation of a high sea surface height signal around the west coast of Iceland (Spall et al., 2017). This would act to maintain a high sea surface height over the Iceland shelf to the east of the trough, even in the presence of upwelling-favorable winds. Thus, the enhanced southward flow of the NIJ/separated EGC due to the negative wind stress curl, lowering the sea surface height in the trough, would be concomitate with a stronger northward-flowing NIIC. These ideas warrant further investigation, but are beyond the scope of the present study.

5. Dynamics in the trough

5.1 Hydraulic criticality

Previous observations have shown that the density structure of the overflow water in Denmark Strait is consistent with that of hydraulic flow over a sill (e.g. Spall and Price, 1998; Nikolopoulos et al., 2003). Despite the fact that the dense water formation in the Nordic Seas is seasonal (e.g. Brakstad et al., 2019), the overflow transport in Denmark Strait shows little to no seasonality (Jochumsen et al., 2012; Harden et al., 2016). Furthermore, the different branches feeding the overflow tend to vary out of phase with each other, such that the total transport remains fairly steady. Together, these results suggest that the overflow through the strait is hydraulically controlled. Using observations and a numerical model, Käse et al. (2003) diagnosed the hydraulic conditions in Denmark Strait using the Froude number $Fr = v/\sqrt{g'D}$, where D is the vertical length scale, $g' = g\ \Delta\rho/\rho$ is the reduced gravity, g is the gravitational acceleration, and $\Delta\rho$ is the density difference across the interface. Käse et al. (2003) considered different parts of the domain and found that the flow upstream of the sill is subcritical ($Fr < 1$), but, as the flow descends into the Irminger Basin and accelerates, it becomes supercritical ($Fr > 1$). The transition location is roughly 100 km downstream of the sill. This is consistent with theory (Pratt, 1986), observations (Price and Baringer, 1994), and other models (Spall and Price, 1998) regarding the subcritical-to-supercritical transition over a sill.

We investigated the Froude number using our 22 sections. In the scenario where the dense water flows beneath a motionless or slowly moving upper layer, the Froude number is the expression given above. In our case, especially for the cyclonic state, there is strong flow throughout the water column. As such, it is more appropriate to use the composite Froude number G for two active layers (Armi, 1986; Kösters, 2004; Pratt, 2008):

$$G^2 = Fr_1^2 + Fr_2^2 \tag{1}$$

where $Fr_n = v_n/\sqrt{g' D_n}$ is the Froude number in the n^{th} layer. The quantity v_n is the vertically-averaged advective speed in layer n, and the denominator is the internal gravity wave speed where D_n is the layer thickness. A two-layer flow that is laterally uniform is considered supercritical when $G > 1$ and subcritical when $G < 1$. For flows with strong lateral variations in layer thickness and velocity, a local value of $G > 1$ indicates that the flow is locally supercritical, but does not necessarily indicate that the flow as a whole is supercritical. In this case, locally generated disturbances will propagate downstream whereas disturbances that exist over the whole channel width may still propagate upstream (Pratt and Helfrich, 2005). Thus, a flow may be supercritical at certain locations but also subcritical as a whole. We choose the 27.8 kg m^{-3} isopycnal as the interface between the two layers, since this is the top of the dense overflow water and also corresponds to the maximum in stratification (see also von Appen et al., 2017).

For each occupation we calculated G at the grid points across the section corresponding to the southward flow. Figure 9 shows the results, where we have distinguished between the cyclonic cases (red) and non-cyclonic cases (blue). The individual realizations are plotted as open circles, and the means for the two cases at each cross-stream location are the solid circles. One sees that, for the cyclonic state, the mean G exceeds 1 on the western flank of the trough where the merged NIJ/separated EGC is strongest (Fig. 6a). In all, 11 out of the 15 cyclonic realizations had G >1 in this part of the strait. By contrast, the mean G for the non-cyclonic state is lower than 1 everywhere, although 4 out of the 7 realizations had a value of G >1 somewhere in the domain. As noted above, models and observations indicate that the overflow plume descending from Denmark Strait reaches hydraulic criticality approximately 100 km downstream of the sill. One is tempted to conclude from our measurements that localized hydraulic criticality also occurs intermittently at the sill itself, in the cyclonic configuration when the merged NIJ/separated EGC is intensified on the western flank of the trough. However, the presence of such a confined region where $G > 1$ does not necessarily imply that strait-wide hydraulic control is occurring (Pratt and Helfrich, 2005). Further work is required to shed light on this.

5.2 Mixing and Potential vorticity

Although it remains unclear if the Denmark Strait sill can act as a location of strait-wide hydraulic control akin to what happens farther south, the strong flow at the Látrabjarg line, in conjunction with the weak stratification, result in another important aspect of supercritical flow – that of mixing. This can be assessed by considering the gradient Richardson number, defined as the ratio of the buoyancy frequency to the square of vertical shear in velocity,

$$Ri = -\frac{g}{\rho_0}\frac{\partial \rho}{\partial z}\left(\frac{\partial u}{\partial z}\right)^{-2}, \tag{2}$$

where ρ is the local density, ρ_o is the background density (section-wide average), and u is the along-strait velocity. When Ri is less than the critical value of 0.25 the flow can be subject to Kelvin-Helmholtz instability, which leads to vertical mixing (in many studies the critical value is taken to be in the range 0.2–1.0; e.g. Galperin et al., 2007). In Figure 10 we show the vertical section of Ri for the July 2007 occupation, which is one of the sections where $G > 1$ within the trough. This reveals a region of $Ri < 0.25$ along the steeply-sloped density front separating the cold overflow water from the warm Irminger Water. In this case both the weak stratification and strong velocity shear contribute to the small value of Ri. It is expected that strong vertical mixing would be occurring in this region.

To further investigate the nature and extent of mixing at the Látrabjarg line, we consider the potential vorticity dynamics of the flow using our 22 occupations. We did this by evaluating the Ertel potential vorticity (e.g. Spall and Pedlosky, 2008; Lin et al., 2018),

$$\Pi = -\frac{f}{\rho_0}\frac{\partial \rho}{\partial z} + \frac{1}{\rho_0}\frac{\partial u}{\partial y}\frac{\partial \rho}{\partial z} - \frac{1}{\rho_0}\frac{\partial u}{\partial z}\frac{\partial \rho}{\partial y} \quad , \tag{3}$$

where the y-direction is cross-strait, positive towards Iceland. The Ertel potential vorticity (PV) has three components: 1) the planetary stretching vorticity term, dictated by the vertical stratification and earth's rotation; 2) the relative vorticity term, due to the combination of the lateral gradient of the horizontal velocity and vertical stratification; and 3) the tilting vorticity term, due to the vertical gradient of horizontal velocity and lateral gradient of density. It is instructive to normalize the second and third terms by the planetary stretching term. For the relative vorticity, this gives

$$R_o = -\frac{1}{f}\frac{\partial u}{\partial y}\,. \tag{4}$$

For the tilting vorticity the ratio is

$$R_z = \frac{g\alpha}{f^2\rho_0}\frac{\partial \rho}{\partial y}\ , \tag{5}$$

where α is the isopycnal slope; to derive this, we used the thermal wind relation, $\frac{\partial u}{\partial z} = \frac{g}{f\rho_0}\frac{\partial \rho}{\partial y}$.

Using a representative length scale L and velocity scale U, the first ratio (Eq. 4) can be expressed as $R_o = \frac{U}{fL}$, which is the Rossby number. Taking ΔU as the change in velocity over the depth scale, the second ratio (Eq. 5) can be expressed as $R_z = \frac{\Delta U}{fL}$, which has the form of a Rossby number associated with the depth variation in velocity; we refer to this as the shear Rossby number. Note that when the flow is barotropic R_z will be small, even though R_o could be large. When the flow is strongly baroclinic R_z could be large.

Returning to the July 2007 occupation, we computed the total Ertel PV and its three components, where the latter two terms have been normalized to show R_o and R_z (Fig. 11). One sees that over most of the section the total PV is qualitatively similar to the stretching term, particularly in the upper layer. However, in the trough the other two terms are significant. The large Rossby number (up to 1.5) changes sign across the merged NIJ/separated EGC, indicating that this flow is highly nonlinear and may be barotropically unstable (Pickart et al., 2005). Furthermore, the lateral gradient of the total PV changes sign with depth in the trough (Fig. 11a), which is a necessary condition for baroclinic instability. This is in line with the model results of Spall et al. (2019) who identified that both the merged NIJ/separated EGC and NIIC are baroclinically unstable. This instability acts to weaken the hydrographic front that is maintained by the convergence of the large scale mean flow.

Note also in Fig. 11 that, due to the steeply-sloped isopycnals of the hydrographic front (and corresponding strong velocity shear via thermal wind), the shear Rossby number is less than -1, i.e. the same order as the Rossby number. This results in regions of negative total PV; in particular, note the correspondence between the strong tilting vorticity in Fig. 11d and negative Π in Fig. 11a. The condition of negative total PV can lead to symmetric instability (Haine and Marshall, 1998; D'Asaro et al., 2011), a fast-growing instability that occurs on the order of a few hours (Brearley et al., 2012). At finite amplitude this results in intense, rapid diapycnal mixing (Haine and Marshall, 1998). We now explore further the signature of symmetric instability in our data.

5.3 Symmetric instability

Based on the July 2007 occupation, we seek to elucidate the relationship between the tilting vorticity, or more specifically R_z, and the occurrence of negative PV. Using all the grid points of the 22 realizations, we regressed R_z against Π (Fig. 12). This shows that when R_z < -1, 73% of the time this corresponds to negative PV (if the threshold is strengthened to -1.5, the percentage of negative PV is 93%). For the remaining 27% of the data points, the strong positive relative vorticity overcomes the tilting vorticity such that the total PV remains positive. This is seen in Fig. 12, where the value of R_o for each data point is indicated using color. The points in question generally have $0.5 < R_o < 1.5$. Alternatively, the color in Fig. 12 reveals that when negative PV does not correspond to R_z < -1 this is due to the flow having a large negative R_o (dark blue symbols in Fig.

12). We thus conclude that, outside of extreme instances of large relative vorticity (of either sign), it is generally the case that when the shear Rossby number is less than -1, the total PV is negative – which will result in symmetric instability. This is consistent with the classification of instability in Thomas et al. (2013).

Part of our rationale for casting the symmetric instability condition in terms of R_z is that this ratio does not depend on the velocity of the flow, but only on the density structure (see Eq. 5). As such, we can extend the application of the proxy to the complete set of historical hydrographic Látrabjarg sections (we exclude 9 short sections that did not cross the trough). We find that R_z < -1 in 60 of the 112 sections, i.e. over 50% of the time (for the more restrictive criterion of R_z < -1.5 it is 42%). This suggests that symmetric instability occurs quite frequently in Denmark Strait. Interestingly, the presence of symmetric instability does not seem to be tied to the cyclonic or non-cyclonic velocity states, or to the presence of boluses versus pulses.

To determine where in the water column the conditions for symmetric instability occur, we tabulated the occurrences of R_z < -1 for all of the sections (Fig. 13). This reveals that the instability occurs mainly in the trough, with a few instances near the surface on the Iceland shelf and near the bottom in the vicinity of the Greenland shelfbreak. However, the majority of cases are clustered into two areas: a deeper region near the western side of the trough, and a shallower region closer to the eastern side of the trough. To shed light on the underlying reasons for this pattern, we constructed a composite hydrographic section for all of the occurrences in the deeper region, then did the same for the shallower region. These are shown in Fig. 14. For the shallower occurrences there is a large amount of cold overflow water filling the trough, while for the deeper occurrences there is only a thin layer of this water banked on the western side of the trough. These two states correspond nearly identically with the hydrographic patterns of boluses and pulses, respectively (von Appen et al., 2017). Note that in both cases the instability takes place in the steep frontal zone, where the tilting vorticity is strongly negative. This result suggests that strong vertical mixing occurs at the top of the overflow layer, regardless of whether there is a large or small amount of dense water present. The implication is that, even though strait-wide hydraulic control may not be achieved until downstream of Denmark Strait, the mixing/entrainment process that modifies the overflow water begins at the sill (also see North et al., 2018).

6. Summary and Discussion

In this study we have used 22 occupations of the Látrabjarg line from 1993–2018, together with reanalysis wind fields and satellite absolute dynamic topography data, to investigate the kinematic structure and dynamics of the Denmark Strait Overflow Water. While the Látrabjarg section has been occupied over 100 times through the years, the unique aspect of the subset considered here is that it includes shipboard velocity data that were used to construct vertical sections of absolute geostrophic velocity. The mean velocity section reveals the presence of the shelfbreak EGC in the vicinity of the Greenland shelf edge, the merged NIJ/separated EGC banked against the western side of the deep trough, and the northward-flowing NIIC near the Iceland shelfbreak.

The mean transport of the overflow water (denser than 27.8 kg m^{-3}) is 3.54 ± 0.29 Sv, which includes an extrapolated estimate of the unresolved component on the Greenland shelf (0.54 Sv). This is close to previously published estimates of the mean overflow transport (Harden et al., 2016; Jochumsen et al., 2017). We partitioned the transport in terms of water masses and current components. For the former we used a hydrographic end-member analysis to distinguish Atlantic-origin Overflow Water (AtOW) from Arctic-origin Overflow Water (ArOW). Assuming that the unresolved overflow transport on the Greenland shelf is AtOW, this gives 1.72 ± 0.15 Sv for

ArOW and 1.49 ± 0.10 Sv for AtOW, indicating that the mean transports of the two types of overflow water are comparable in Denmark Strait. For the currents, we distinguished the shelfbreak EGC and the merged NIJ/separated EGC using a geographical boundary, and assumed that the unresolved overflow water on the Greenland shelf emanated from the shelfbreak EGC upstream of the strait. This gives 1.39 ± 0.14 Sv for the shelfbreak EGC and 2.15 ± 0.15 Sv for the merged flow, which is in line with similar partitioning done by Harden et al. (2016) upstream in the Blosseville Basin. Notably, both currents transport both types of overflow water, implying a significant degree of exchange between the branches as they converge in Denmark Strait.

With regard to temporal variability, there were two dominant configurations of the flow which we refer to as the cyclonic state and the non-cyclonic state. The former is characterized by a strong southward flow of the merged NIJ/separated EGC adjacent to a strong northward flow of the NIIC. This structure was present in 15 of the 22 occupations. In this state the NIIC is located farther to the west and occupies part of the trough. The remaining 7 sections corresponded to weaker southward and northward flows, with the NIIC shifted eastward and the entire trough associated with the merged NIJ/separated EGC. Using the reanalysis wind data, it was demonstrated that the cyclonic state corresponds to negative wind stress curl north of the strait in the Blosseville Basin and strong northeasterly winds within the strait. The former is conducive for an enhanced merged flow as demonstrated previously (Våge et al., 2013). Using the satellite surface geostrophic velocity data, we showed that the NIIC becomes stronger and shifts closer to the shelfbreak under northeasterly winds, although the physical mechanism for this remains unresolved.

The hydraulic criticality of the flow was assessed using a composite Froude number that can account for two moving layers – the overflow layer and the lighter water above. This revealed that roughly two thirds of the cyclonic realizations had regions of super-critical flow in the trough, and this condition was present in the mean for the strongest flow in the merged NIJ/separated EGC. This suggests that hydraulic control could be occurring intermittently during the cyclonic state. However, the presence of such a confined region of large Froude number does not necessarily imply that strait-wide hydraulic control is occurring (Pratt and Helfrich, 2005).

A potential vorticity (PV) analysis of the 22 occupations indicated that the flow through Denmark Strait is subject to symmetric instability. This occurs when the total PV is negative, which tends to happen when the tilting vorticity becomes strongly negative. We determined that the shear Rossby number (R_z) is a good proxy for determining when symmetric instability is active. In particular, when R_z is less than -1, the total PV is typically negative. This proxy, which does not rely on the flow speed but only the density structure, was then applied to the full set of 122 Látrabjarg occupations. This revealed that symmetric instability tends to occur at the top of the overflow layer, regardless of whether there is a large or small amount of dense water in the strait. Symmetric instability is a fast-growing instability that reaches finite amplitude in a matter of hours, leading to intense vertical mixing. This implies that, even though hydraulic criticality may not be achieved until downstream of the strait, the mixing/entrainment process that modifies the overflow water begins at the sill.

Previous work has implied that the dominant mesoscale variability in Denmark Strait is due to baroclinic instability of the hydrographic front that separates the overflow water from the subtropical-origin water in the NIIC (Spall et al., 2019). The resulting meanders of the front propagate equatorward through the strait and are associated with the well-known boluses and pulses of overflow water (Mastropole et al., 2017; von Appen et al., 2017). In particular, meander crests are associated with boluses, which correspond to thick layer of overflow water, whereas meander troughs coincide with pulses, which are characterized by a thin layer of overflow water.

The results presented here suggest that the dominant variation in alongstream velocity at the sill is wind-driven, rather than being associated with the amount of overflow water present. There are several factors that may help explain this apparent discrepancy.

The numerical model results of Almansi et al. (2017) show that, relative to the background state, the biggest difference in the alongstream velocity signature of the boluses and pulses is the bottom intensification associated with the latter. While we don't have enough realizations of the Látrabjarg section with velocity to determine a background state, our composite of pulse realizations shows significantly more bottom-intensification in the trough versus the composite of bolus realizations, in line with Almansi et al.'s (2017) results. Another thing to keep in mind is that the mooring analysis of von Appen et al. (2017) showed that the most conspicuous difference between the passage of boluses versus pulses pertains to the cross-stream velocity signal (cyclonic for boluses, anti-cyclonic for pulses), which we are unable to assess. Both features were associated with an enhancement of the alongstream velocity in the overflow layer. The maximum flow in von Appen et al.'s (2017) bolus composite exceeded 0.40 m s^{-1}, while that for their pulse composite exceeded 0.60 m s^{-1}. In our composite vertical sections, the mean near-bottom flow of the pulses is only slightly larger than for the boluses (0.30 m s^{-1} versus 0.24 m s^{-1}), but it must be kept in mind that the mooring composites were based on vastly more data. In any event, both the shear and the magnitude of the alongstream flow – together with the strong hydrographic signals – suggest that we indeed detect these mesoscale features.

A final consideration regarding the velocity variability seen in our dataset is the short timescale associated with the passage of the boluses and pulses. The mooring composites of von Appen et al. (2017) indicate that, for both types of features, the strongest signals in alongstream velocity persist for approximately 12 hours. Typical occupations of the Látrabjarg line take a day or more to complete. This means that the timing has to be perfect for a shipboard transect to capture the peak alongstream velocity signature of one these mesoscale features in the trough. On the other hand, the wind-driven flow variability takes place over longer timescales. The ERA5 data indicate that the auto-correlation time for the along-strait winds is 73 hours. Therefore, it is more likely that a given transect will be under the influence of a single wind state. As the collection of Látrabjarg occupations with velocity continues to increase over time, we will be better positioned to elucidate the impacts of external versus internal forcing of the overflow water.

Acknowledgements

An inordinate amount of effort was required to obtain, processes, and quality-control the data used in this study. The authors are thankful for the efforts of the many individuals, both at sea and ashore, that made the analysis possible. We are also indebted to M. Spall, T. Haine, and S. Tan for invaluable discussions and insights. Funding for the study was provided by National Science Foundation (NSF) grants OCE-1259618, OCE-1756361, and OCE-1558742. The German research cruises were financially supported through various EU Projects (e.g. THOR, NACLIM) and national projects (most recently TRR 181 "Energy Transfer in Atmosphere and Ocean" funded by the German Research Foundation and RACE II "Regional Atlantic Circulation and Global Change" funded by the German Federal Ministry for Education and Research). GWKM acknowledges the support of the Natural Sciences and Engineering Research Council of Canada. LP was supported by NSF Grant OCE-1657870.

References

Almansi, M., T. Haine, R. Gelderloos, and R. Pickart, 2020: Evolution of Denmark Strait Overflow Cyclones and Their Relationship to Overflow Surges, *Geophys. Res. Lett.*

Almansi, M., T. W. Haine, R. S. Pickart, M. G. Magaldi, R. Gelderloos, and D. Mastropole, 2017: High-frequency variability in the circulation and hydrography of the Denmark Strait overflow from a high-resolution numerical model, *J. Phys. Oceanogr.*, 47(12), 2999-3013.

Brakstad, A., K. Våge, L. Håvik, and G. Moore, 2019: Water mass transformation in the Greenland Sea during the period 1986–2016, *J. Phys. Oceanogr.*, 49(1), 121-140.

Brearley, J. A., R. S. Pickart, H. Valdimarsson, S. Jonsson, R. W. Schmitt, and T. W. Haine, 2012: The East Greenland boundary current system south of Denmark Strait, *Deep Sea Res. I*, 63, 1-19.

Casanova-Masjoan, M, M.D Pérez-Hernández, R.S. Pickart, H. Valdimarsson, A. Macrander, P. Vélez-Belchí, D. Grisolía-Santos, D. J. Torres, S. Jonsson, K. Våge, A. Hernández-Guerra. Alongstream, seasonal and interannual variability of the North Icelandic Irminger Current and East Icelandic Current around Iceland. Submitted.

D'Asaro, E., C. Lee, L. Rainville, R. Harcourt, and L. Thomas, 2011: Enhanced turbulence and energy dissipation at ocean fronts, *science*, 332(6027), 318-322.

de Steur, L., E. Hansen, R. Gerdes, M. Karcher, E. Fahrbach, and J. Holfort, 2009: Freshwater fluxes in the East Greenland Current: A decade of observations, *Geophys. Res. Lett.*, 36(23).

Dickson, R. R., and J. Brown, 1994: The production of North Atlantic Deep Water: sources, rates, and pathways, *J. Geophys. Res. Oceans*, 99(C6), 12319-12341.

Galperin, B., S. Sukoriansky, and P. S. Anderson, 2007: On the critical Richardson number in stably stratified turbulence, *Atmospheric Science Letters*, 8(3), 65-69.

Girton, J. B., and T. B. Sanford, 2003: Descent and modification of the overflow plume in the Denmark Strait, *J. Phys. Oceanogr.*, 33(7), 1351-1364.

Haine, T. W., and J. Marshall, 1998: Gravitational, symmetric, and baroclinic instability of the ocean mixed layer, *J. Phys. Oceanogr.*, 28(4), 634-658.

Harden, B. E., R. S. Pickart, H. Valdimarsson, K. Våge, L. de Steur, C. Richards, F. Bahr, D. Torres, E. Børve, and S. Jónsson, 2016: Upstream sources of the Denmark Strait Overflow: Observations from a high-resolution mooring array, *Deep Sea Res. I*, 112, 94-112.

Håvik, L., R. S. Pickart, K. Våge, D. Torres, A. M. Thurnherr, A. Beszczynska-Möller, W. Walczowski, and W. J. von Appen, 2017a: Evolution of the East Greenland Current from Fram Strait to Denmark Strait: synoptic measurements from summer 2012, *J. Geophys. Res. Oceans*, 122(3), 1974-1994.

Håvik, L., K. Våge, R. Pickart, B. Harden, W.-J. v. Appen, S. Jónsson, and S. Østerhus, 2017b: Structure and variability of the shelfbreak East Greenland Current north of Denmark Strait, *J. Phys. Oceanogr.*, 47(10), 2631-2646.

Holte, J., and F. Straneo, 2017: Seasonal overturning of the Labrador Sea as observed by Argo floats, *J. Phys. Oceanogr.*, 47(10), 2531-2543.

Høyer, J. L., and D. Quadfasel, 2001: Detection of deep overflows with satellite altimetry, *Geophys. Res. Lett.*, 28(8), 1611-1614.

Huang, J., R. S. Pickart, H. Valdimarsson, P. Lin, M. A. Spall, and F. Xu, 2019: Structure and variability of the North Icelandic Jet from two years of mooring data, *J. Geophys. Res. Oceans*, 124(6), 3987-4002.

Huang, J., R. S. Pickart, R. X. Huang, P. Lin, A. Brakstad, and F. Xu. Sources and upstream pathways of the densest overflow in the Nordic Seas. Submitted.

Jochumsen, K., M. Moritz, N. Nunes, D. Quadfasel, K. M. Larsen, B. Hansen, H. Valdimarsson, and S. Jonsson, 2017: Revised transport estimates of the D enmark S trait overflow, *J. Geophys. Res. Oceans*, 122(4), 3434-3450.

Jochumsen, K., D. Quadfasel, H. Valdimarsson, and S. Jónsson, 2012: Variability of the Denmark Strait overflow: Moored time series from 1996–2011, *J. Geophys. Res. Oceans*, 117(C12).

Käse, R. H., J. Girton, and T. Sanford, 2003: Structure and variability of the Denmark Strait Overflow: Model and observations, *J. Geophys. Res. Oceans*, 108(C6).

Kösters, F., 2004: Denmark Strait overflow: Comparing model results and hydraulic transport estimates, *J. Geophys. Res. Oceans*, 109(C10).

Lin, P., R. S. Pickart, D. J. Torres, and A. Pacini, 2018: Evolution of the freshwater coastal current at the southern tip of Greenland, *J. Phys. Oceanogr.*, 48(9), 2127-2140.

Logemann, K., J. Ólafsson, Á. Snorrason, H. Valdimarsson, and G. Marteinsdóttir, 2013: The circulation of Icelandic waters-a modelling study, *Ocean Science Discussions*, 10(2).

Lozier, M., F. Li, S. Bacon, F. Bahr, A. Bower, S. Cunningham, M. De Jong, L. De Steur, B. Deyoung, and J. Fischer, 2019: A sea change in our view of overturning in the subpolar North Atlantic, *Science*, 363(6426), 516-521.

Macrander, A. (2004), Variability and processes of the Denmark Strait overflow, Christian-Albrechts-Universität.

Mastropole, D., R. S. Pickart, H. Valdimarsson, K. Våge, K. Jochumsen, and J. Girton, 2017: On the hydrography of D enmark S trait, *J. Geophys. Res. Oceans*, 122(1), 306-321.

Mauritzen, C., 1996: Production of dense overflow waters feeding the North Atlantic across the Greenland-Scotland Ridge. Part 1: Evidence for a revised circulation scheme, *Deep Sea Res. I*, 43(6), 769-806.

Moritz, M., K. Jochumsen, R. P. North, D. Quadfasel, and H. Valdimarsson, 2019: Mesoscale Eddies observed at the Denmark Strait sill, *J. Geophys. Res. Oceans*, 124(11), 7947-7961.

Nikolopoulos, A., K. Borenäs, R. Hietala, and P. Lundberg, 2003: Hydraulic estimates of Denmark Strait overflow, *J. Geophys. Res. Oceans*, 108(C3).

Nikolopoulos, A., R. S. Pickart, P. S. Fratantoni, K. Shimada, D. J. Torres, and E. P. Jones, 2009: The western Arctic boundary current at 152°W: Structure, variability, and transport, *Deep Sea Research II*, 56(17), 1164-1181, doi:10.1016/j.dsr2.2008.10.014.

North, R. P., K. Jochumsen, and M. Moritz, 2018: Entrainment and energy transfer variability along the descending path of the Denmark Strait overflow plume, *J. Geophys. Res. Oceans*, 123(4), 2795-2807.

Pickart, R. S., G. Moore, C. Mao, F. Bahr, C. Nobre, and T. J. Weingartner, 2016: Circulation of winter water on the Chukchi shelf in early Summer, *Deep Sea Res. II*, 130, 56-75.

Pickart, R. S., and M. A. Spall, 2007: Impact of Labrador Sea convection on the North Atlantic meridional overturning circulation, *J. Phys. Oceanogr.*, 37(9), 2207-2227.

Pickart, R. S., M. A. Spall, D. J. Torres, K. Våge, H. Valdimarsson, C. Nobre, G. Moore, S. Jonsson, and D. Mastropole, 2017: The North Icelandic Jet and its relationship to the North Icelandic Irminger Current, *J. Mar. Res.*, 75(5), 605-639.

Pickart, R. S., D. J. Torres, and P. S. Fratantoni, 2005: The east Greenland spill jet, *J. Phys. Oceanogr.*, 35(6), 1037-1053.

Pratt, L. J., 1986: Hydraulic control of sill flow with bottom friction, *J. Phys. Oceanogr.*, 16(11), 1970-1980.

Pratt, L. J., 2008: Critical conditions and composite Froude numbers for layered flow with transverse variations in velocity, *Journal of Fluid Mechanics*, 605, 281-291.

Price, J. F., and M. O. N. Baringer, 1994: Outflows and deep water production by marginal seas, *Prog. Oceanogr.*, 33(3), 161-200.

Rudels, B., G. Björk, J. Nilsson, P. Winsor, I. Lake, and C. Nohr, 2005: The interaction between waters from the Arctic Ocean and the Nordic Seas north of Fram Strait and along the East Greenland Current: results from the Arctic Ocean-02 Oden expedition, *J. Mar. Syst.*, 55(1), 1-30.

Rudels, B., P. Eriksson, H. Grönvall, R. Hietala, and J. Launiainen, 1999: Hydrographic observations in Denmark Strait in fall 1997, and their implications for the entrainment into the overflow plume, *Geophys. Res. Lett.*, 26(9), 1325-1328.

Pratt, L., and K. Helfrich, 2005: Generalized conditions for hydraulic criticality of oceanic overflows, *J. Phys. Oceanogr.*, 35(10), 1782-1800.

Semper, S., K. Våge, R. S. Pickart, H. Valdimarsson, D. J. Torres, and S. Jónsson, 2019: The emergence of the North Icelandic Jet and its evolution from northeast Iceland to Denmark Strait, *J. Phys. Oceanogr.*, 49(10), 2499-2521.

Smith, P. C., 1976: Baroclinic instability in the Denmark Strait overflow, *J. Phys. Oceanogr.*, 6(3), 355-371.

Spall, M. A., and J. Pedlosky, 2008: Lateral coupling in baroclinically unstable flows, *J. Phys. Oceanogr.*, 38(6), 1267-1277.

Spall, M. A., J. Pedlosky, and C. Cenedese, 2017: Circulation induced by isolated dense water formation over closed topographic contours, *J. Phys. Oceanogr.*, 47(9), 2251-2265.

Spall, M. A., R. S. Pickart, P. Lin, W.-J. v. Appen, D. Mastropole, H. Valdimarsson, T. W. Haine, and M. Almansi, 2019: Frontogenesis and variability in Denmark Strait and its influence on overflow water, *J. Phys. Oceanogr.*, 49(7), 1889-1904.

Spall, M. A., and J. F. Price, 1998: Mesoscale variability in Denmark Strait: The PV outflow hypothesis, *J. Phys. Oceanogr.*, 28(8), 1598-1623.

Thomas, L. N., J. R. Taylor, R. Ferrari, and T. M. Joyce, 2013: Symmetric instability in the Gulf Stream, *Deep Sea Res. II*, 91, 96-110.

Våge, K., G. W. K. Moore, S. Jónsson, and H. Valdimarsson, 2015: Water mass transformation in the Iceland Sea, *Deep Sea Res. I*, 101, 98-109.

Våge, K., R. S. Pickart, M. A. Spall, G. Moore, H. Valdimarsson, D. J. Torres, S. Y. Erofeeva, and J. E. Ø. Nilsen, 2013: Revised circulation scheme north of the Denmark Strait, *Deep Sea Res. I*, 79, 20-39.

Våge, K., R. S. Pickart, M. A. Spall, H. Valdimarsson, S. Jónsson, D. J. Torres, S. Østerhus, and T. Eldevik, 2011: Significant role of the North Icelandic Jet in the formation of Denmark Strait overflow water, *Nature Geoscience*, 4(10), 723.

von Appen, W., D. Mastropole, R. S. Pickart, H. Valdimarsson, S. Jónsson, and J. B. Girton, 2017: On the nature of the mesoscale variability in Denmark Strait, *J. Phys. Oceanogr.*, 47(3), 567-582.

Whitehead, J., 1989: Internal hydraulic control in rotating fluids—Applications to oceans, *Geophysical & Astrophysical Fluid Dynamics*, 48(1-3), 169-192.

Whitehead, J., A. Leetmaa, and R. Knox, 1974: Rotating hydraulics of strait and sill flows, *Geophysical and Astrophysical Fluid Dynamics*, 6(2), 101-125.

Tables

Table 1. Occupations of the 22 Látrabjarg transects with velocity measurements used in the study (VMADCP: vessel-mounted ADCP; LADCP: lowered ADCP). The 11 occupations marked with an asterisk denote the sections added to the Mastropole et al. (2017) dataset.

Cruise	Ship	Year	date	ADCP
WOCE-93*	R/V *Aranda*	1993	Aug 30	VMADCP
MSM05-4	R/V *Maria S. Merian*	2007	Jul 12 – 13	VMADCP
KN194	R/V *Knorr*	2008	Oct 13 – 14	VMADCP
BS010	R/V *Bjarni Saemundsson*	2009	Aug 11 – 12	LADCP
M82-1	R/V Meteor	2010	Jul 07	VMADCP
BS001	R/V *Bjarni Saemundsson*	2011	Feb 10	LADCP
M85-2	R/V *Meteor*	2011	Aug 19 – 21	VMADCP
KN203	R/V *Knorr*	2011	Aug 22 – 24	VMADCP
BS002	R/V *Bjarni Saemundsson*	2012	Feb 08 – 09	LADCP
MSM21-1b	R/V *Maria S. Merian*	2012	Jun 10 – 11	VMADCP

JR267	R/V *James Clark Ross*	2012	Jul 28 – 29	LADCP
P437	R/V *Poseidon*	2012	Aug 10 – 12	VMADCP
BS013*	R/V *Bjarni Saemundsson*	2013	Feb 06 – 07	LADCP
P471-2*	R/V *Poseidon*	2014	Jul 06 – 08	VMADCP
P486*	R/V *Poseidon*	2015	Jun 14 – 25	VMADCP
BS015*	R/V *Bjarni Saemundsson*	2015	Aug 24	LADCP
P503*	R/V *Poseidon*	2016	Aug 04 – 06	VMADCP
BS017*	R/V *Bjarni Saemundsson*	2017	Aug 05 – 06	LADCP
64PE426*	R/V *Pelagia*	2017	Sep 16 – 18	VMADCP
ALL0118*	NRV *Alliance*	2018	Mar 20 – 21	VMADCP
MSM76*	R/V *Maria S. Merian*	2018	Aug 14 – 15	VMADCP
AR306*	R/V *Armstrong*	2018	Oct 01	VMADCP

Table 2. Partitioning of the DSOW transport (Sv) by water masses and current components. The values in parentheses include the unresolved portion on the Greenland shelf (0.54 Sv).

Currents / Water masses	Shelfbreak EGC	Merged NIJ/separated EGC	Total
Arctic-origin Water	0.41 ± 0.06	1.31 ± 0.09	1.72 ± 0.15
Atlantic-origin Water	0.33 ± 0.06	0.62 ± 0.04	0.95 ± 0.10 (1.49 ± 0.10)
Other water masses	0.11 ± 0.02	0.22 ± 0.02	0.33 ± 0.04
Total	0.85 ± 0.14 (1.39 ± 0.14)	2.15 ± 0.15	3.00 ± 0.29 (3.54 ± 0.29)

Figure captions

Figure 1. Schematic circulation in the vicinity of Denmark Strait, including the two branches of the East Greenland Current (EGC) – the shelfbreak EGC and separated EGC – as well as the North Icelandic Jet (NIJ) and the North Icelandic Irminger Current (NIIC). The blue line across Denmark Strait is the Látrabjarg transect from Mastropole et al. (2017). The bathymetry is from ETOPO2v2. Bathymetry contours are in meters.

Figure 2. Locations of the hydrographic and satellite measurements used in the study. The red dots are the CTD stations. There are a total of 122 CTD sections (many of them overlap, hence the dense clustering of red dots). The Látrabjarg transect from Mastropole et al. (2017) is the black line. The blue dots are the absolute dynamic topography (ADT) altimeter measurements.

Figure 3. Temporal distribution of the 122 Látrabjarg hydrographic sections. Those occupations that include velocity measurements are colored red (for vessel-mounted ADCP data) and magenta (for lowered ADCP). The blue circles correspond to hydrographic measurements only.

Figure 4. Mean vertical sections of the 22 occupations of the Látrabjarg transect. (a) data coverage, (b) potential temperature (°C), (c) salinity, and (d) absolute geostrophic velocity (m s^{-1}) overlain by potential density (kg m^{-3}) contours. Positive (negative) velocities are equatorward (poleward). The highlighted isopycnal of 27.8 kg m^{-3} is the upper boundary of the overflow water. The Iceland shelf is on the east side of the trough (positive distance), and the Greenland shelf is on the west side (negative distance).

Figure 5. Mean vertical sections of the percent presence of the end-member for (a) ArOW and (b) AtOW. The highlighted isopycnal of 27.8 kg m^{-3} is the upper boundary of the overflow water.

Figure 6. Composites of absolute geostrophic velocity (m s-1, color) overlain by potential density (kg m-3, contours) for the (a) cyclonic and (b) non-cyclonic cases. Positive velocities are equatorward. The highlighted isopycnal of 27.8 kg m-3 is the upper boundary of the overflow water. The data coverage is shown on the top panels.

Figure 7. Composites of wind stress curl (× 10-6 N m-3, color) and wind vectors (see the key) for the five extreme cases of (a) strong and (b) weak lateral gradient of depth-mean velocity across the Denmark Strait trough. The green line denotes the Látrabjarg transect. The trough is marked by the red star.

Figure 8. Composites of along-strait surface geostrophic velocity (right column, m s-1) corresponding to different wind conditions in Denmark Strait (left column). The shading represents the standard error. (a) Average of all instances where the northeasterly wind in the strait is greater than the mean plus one standard deviation. (b) Instances where the wind is close to the mean. (c) Instances where the southwesterly wind is greater than the mean plus one standard deviation.

Figure 9. Composite Froude number G as a function of across-strait distance, for the cyclonic cases (red) and anti-cyclonic cases (blue). The individual values for the 22 occupations are open circles, and the mean values at each location are the filled circles. The critical value of $G = 1$ is indicated by the dashed line. The bottom panel shows the bathymetry.

Figure 10. Vertical sections of (a) gradient Richardson number (color) and (b) absolute geostrophic velocity (m s^{-1}; color) overlain by potential density (kg m^{-3}; contours) for the Látrabjarg occupation in July, 2007. The highlighted isopycnal of 27.8 kg m^{-3} is the upper boundary of the overflow water. The inverted triangles indicate the station locations.

Figure 11. Vertical sections of the components of the Ertel potential vorticity (color) for the July 2007 Látrabjarg occupation, overlain by potential density (kg m^{-3}; contours). (a) Total potential vorticity (m^{-1} s^{-1} $\times$ 10^{-10}). (b) Stretching vorticity (m^{-1} s^{-1} $\times$ 10^{-10}). (c) The ratio of relative vorticity to stretching vorticity (R_o). (d) The ratio of tilting vorticity to stretching vorticity (R_z). The highlighted isopycnal of 27.8 kg m^{-3} is the upper boundary of the overflow water. The inverted triangles indicate the station locations.

Figure 12. Scatter plot of the shear Rossby number R_z versus total the potential vorticity Π, using the 22 Látrabjarg sections with velocity. The data points are colored by the value of the Rossby number R_o except for cases when R_z > -1 and Π> 0, which are shaded grey. The black line with open circles is the average value of R_z when it is less than -1, for each PV bin (bin size of 0.4 m^{-1} s^{-1} $\times$ 10^{-10}). The standard errors are included.

Figure 13. Occurrence of symmetric instability for the 122 hydrographic Látrabjarg sections, colored by number of realizations.

Figure 14. Composite average sections of potential temperature (°C, color) overlain by potential density (kg m^{-3}, contours) corresponding to the (a) shallow and (b) deep regions of high occurrence of symmetric instability in Fig. 13. The highlighted isopycnal of 27.8 kg m^{-3} is the upper boundary of the overflow water.

Figures

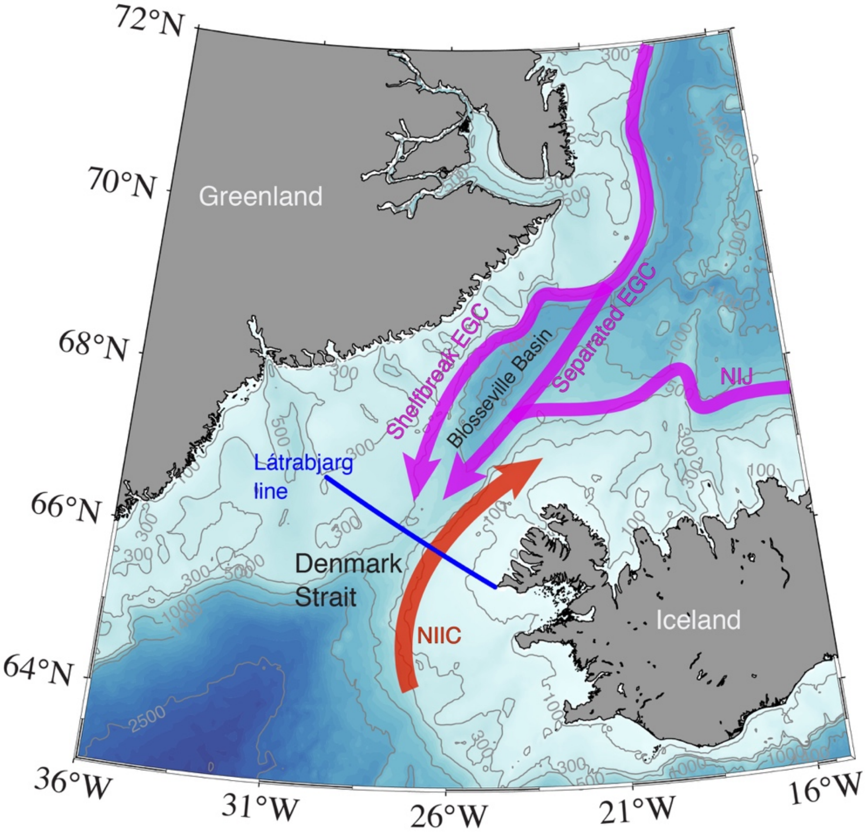

Figure 1. Schematic circulation in the vicinity of Denmark Strait, including the two branches of the East Greenland Current (EGC) – the shelfbreak EGC and separated EGC – as well as the North Icelandic Jet (NIJ) and the North Icelandic Irminger Current (NIIC). The blue line across Denmark Strait is the Látrabjarg transect from Mastropole et al. (2017). The bathymetry is from ETOPO2v2. Bathymetry contours are in meters.

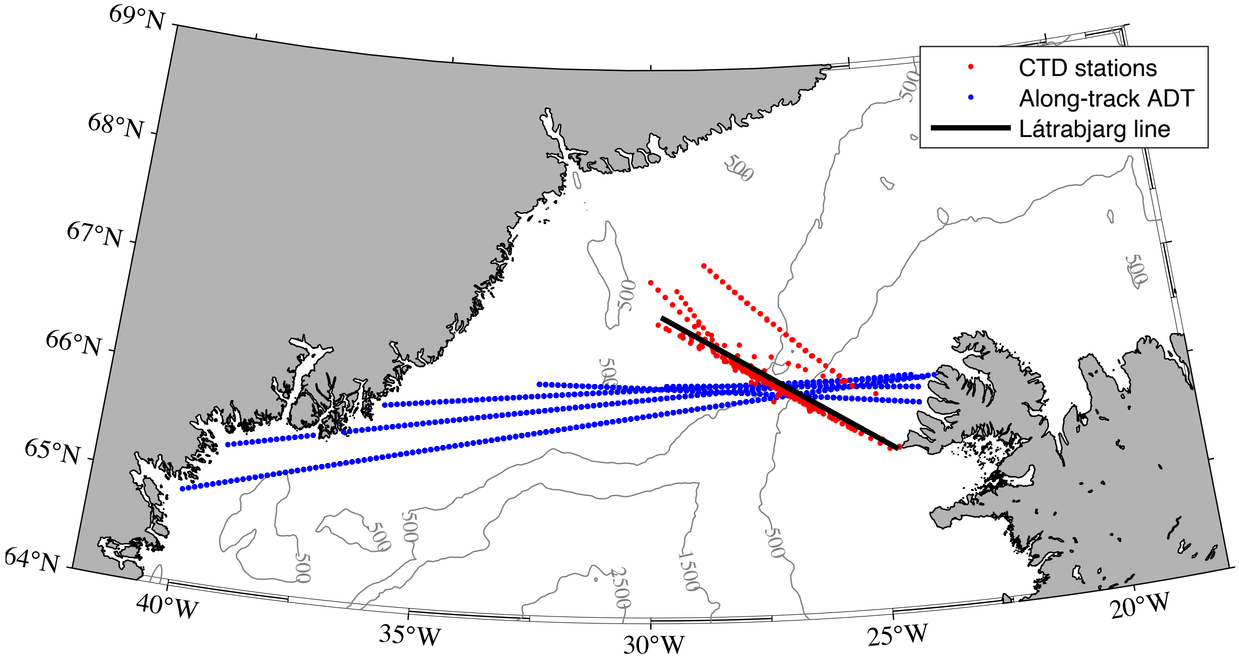

Figure 2. Locations of the hydrographic and satellite measurements used in the study. The red dots are the CTD stations. There are a total of 122 CTD sections (many of them overlap, hence the dense clustering of red dots). The Látrabjarg transect from Mastropole et al. (2017) is the black line. The blue dots are the absolute dynamic topography (ADT) altimeter measurements.

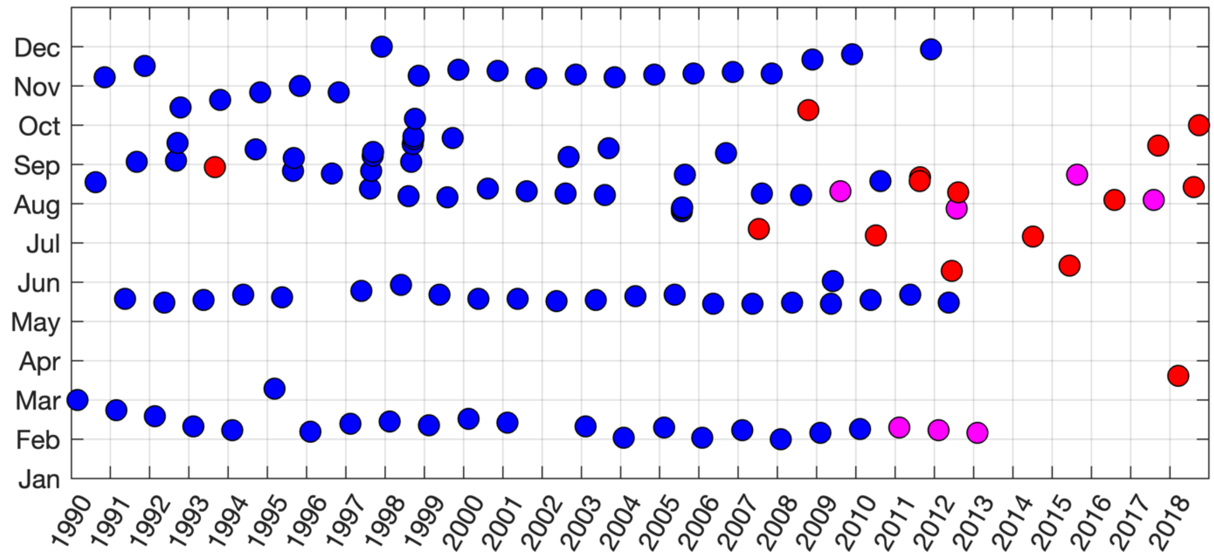

Figure 3. Temporal distribution of the 122 Látrabjarg hydrographic sections. Those occupations that include velocity measurements are colored red (for vessel-mounted ADCP data) and magenta (for lowered ADCP). The blue circles correspond to hydrographic measurements only.

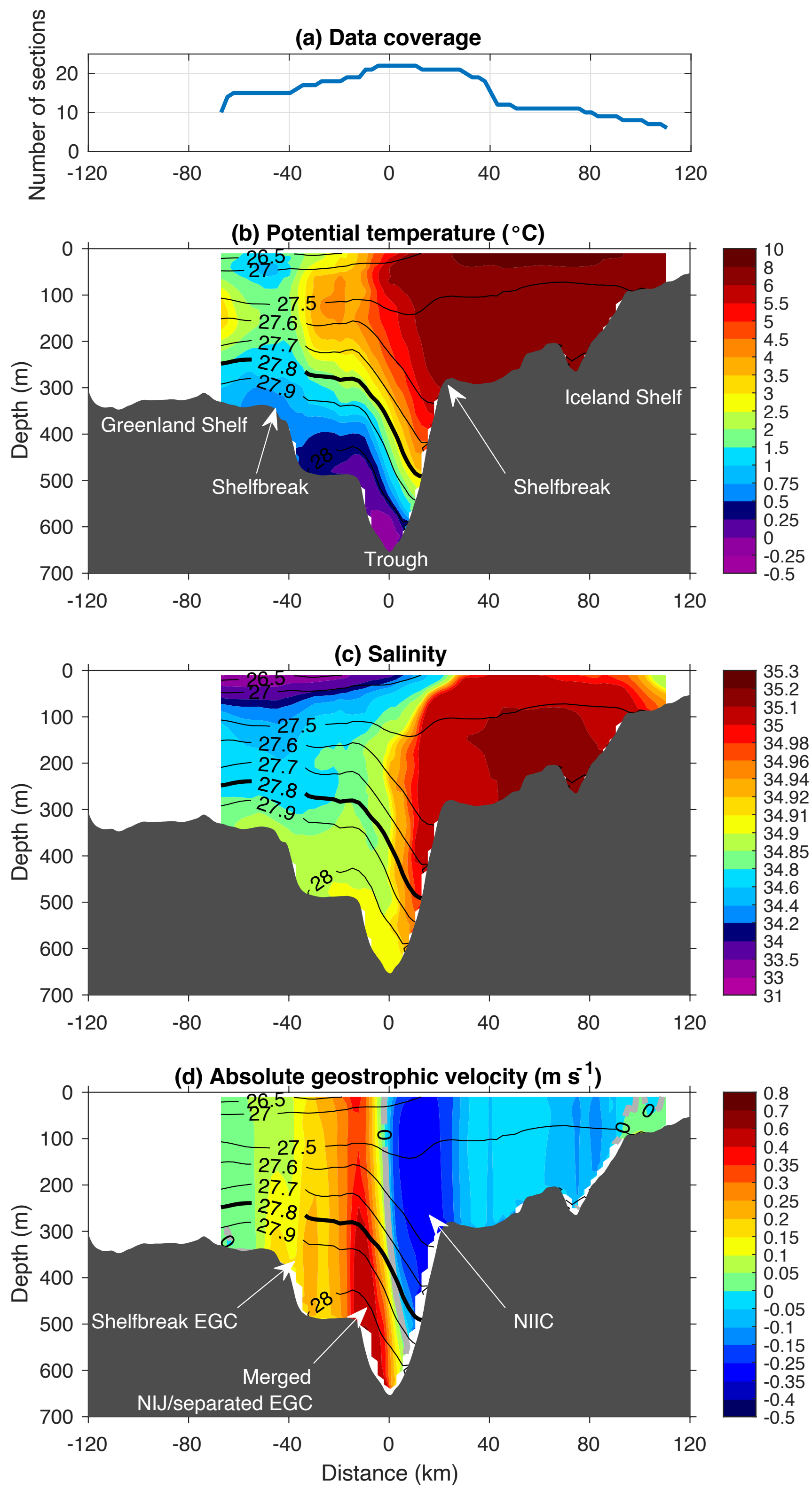
(a) Data coverage
Number of sections
(b) Potential temperature (°C)
Greenland Shelf
Shelfbreak
Trough
Shelfbreak
Iceland Shelf
(c) Salinity
(d) Absolute geostrophic velocity (m s-1)
Shelfbreak EGC
Merged
NIJ/separated EGC
NIIC
Depth (m)
Distance (km)

849

Figure 4. Mean vertical sections of the 22 occupations of the Látrabjarg transect. (a) data coverage, (b) potential temperature (°C), (c) salinity, and (d) absolute geostrophic velocity (m s^{-1}) overlain by potential density (kg m^{-3}) contours. Positive (negative) velocities are equatorward (poleward). The highlighted isopycnal of 27.8 kg m^{-3} is the upper boundary of the overflow water. The Iceland shelf is on the east side of the trough (positive distance), and the Greenland shelf is on the west side (negative distance).

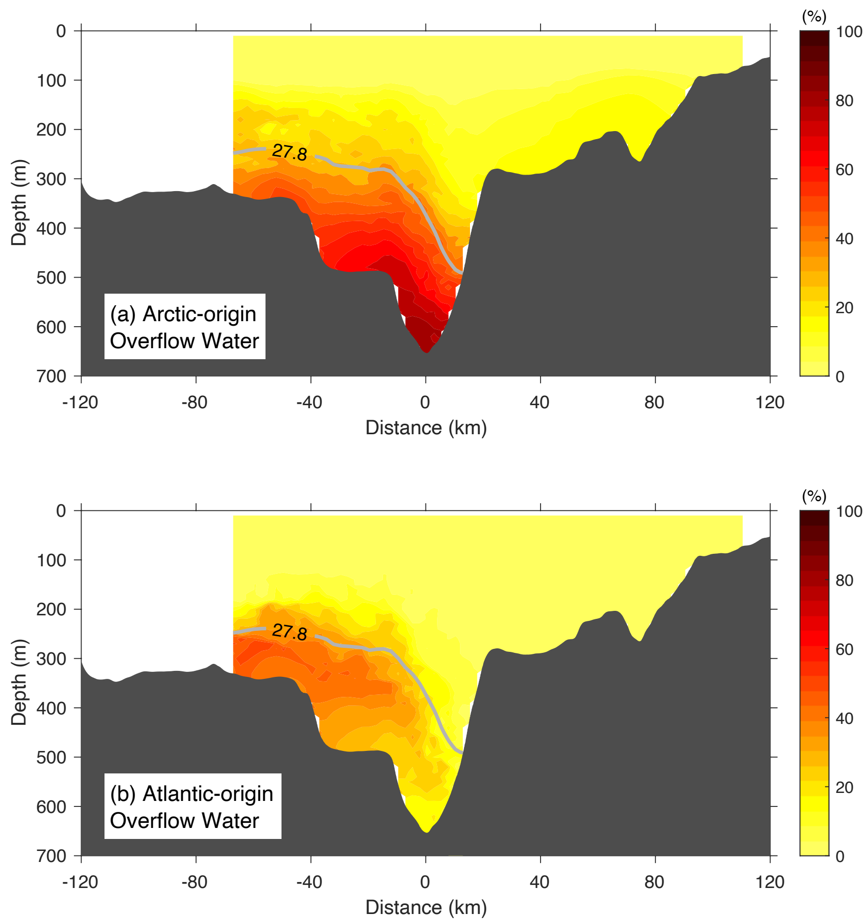

Figure 5. Mean vertical sections of the percent presence of the end-member for (a) ArOW and (b) AtOW. The highlighted isopycnal of 27.8 kg m^{-3} is the upper boundary of the overflow water.

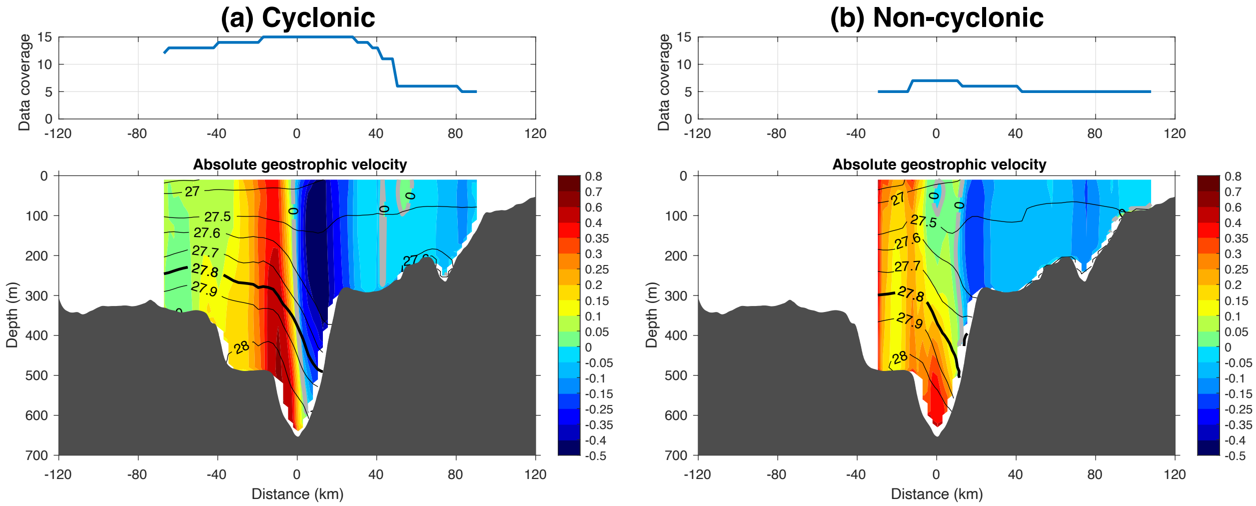

Figure 6. Composites of absolute geostrophic velocity (m s^{-1}, color) overlain by potential density (kg m^{-3}, contours) for the (a) cyclonic and (b) non-cyclonic cases. Positive velocities are equatorward. The highlighted isopycnal of 27.8 kg m^{-3} is the upper boundary of the overflow water. The data coverage is shown on the top panels.

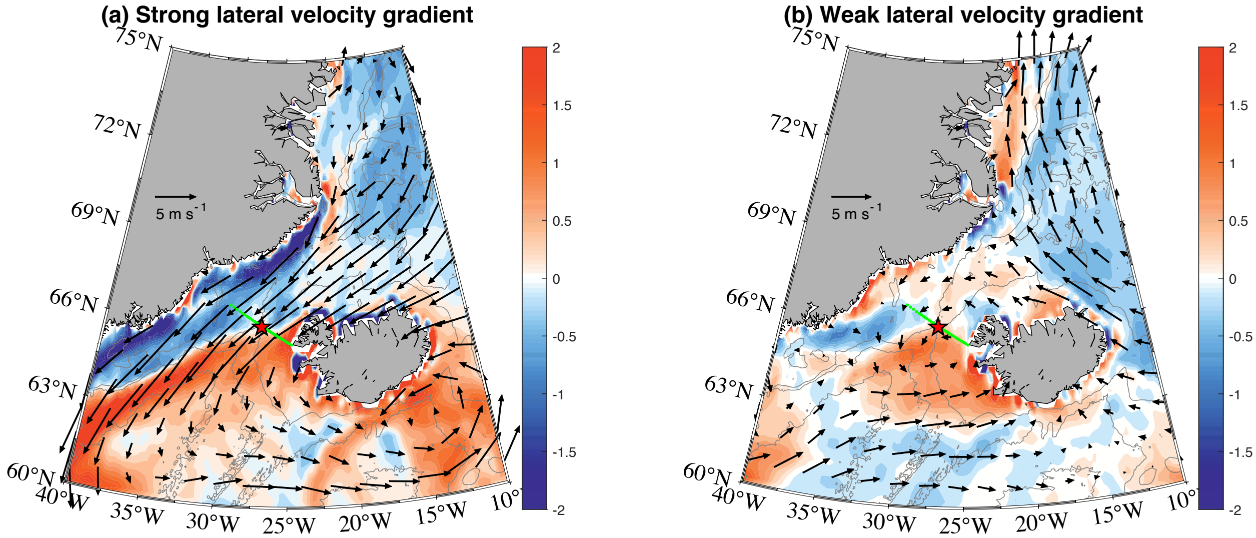

Figure 7. Composites of wind stress curl (× 10^{-6} N m^{-3}, color) and wind vectors (see the key) for the five extreme cases of (a) strong and (b) weak lateral gradient of depth-mean velocity across the Denmark Strait trough. The green line denotes the Látrabjarg transect. The trough is marked by the red star.

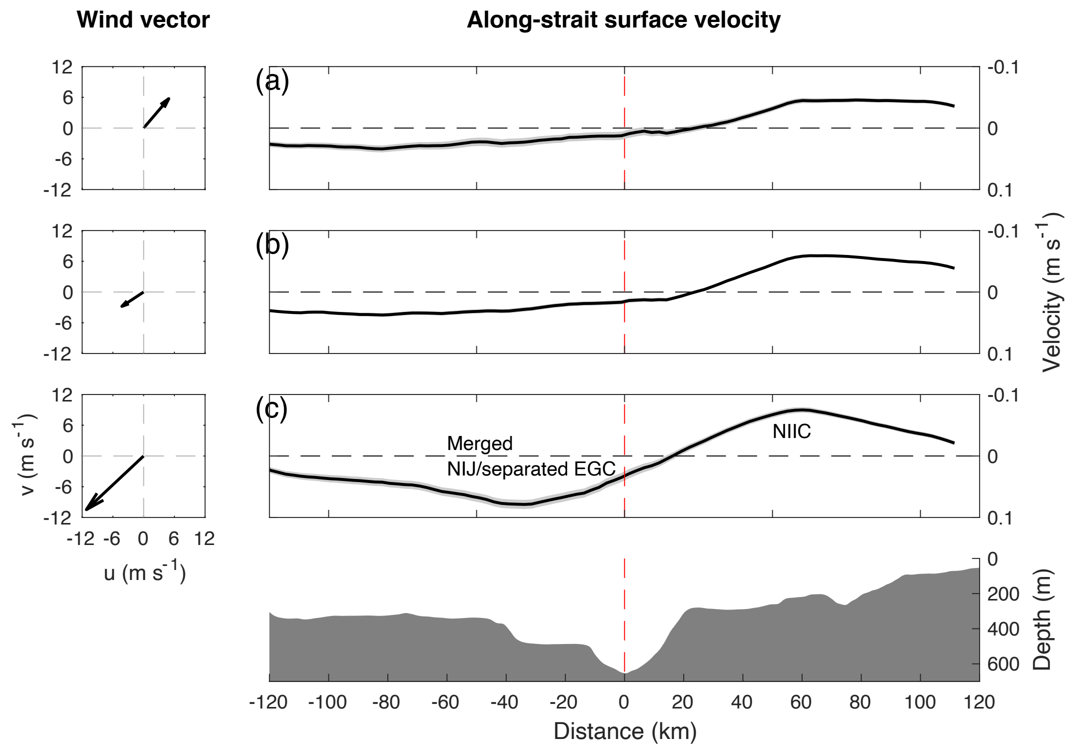

Figure 8. Composites of along-strait surface geostrophic velocity (right column, m s^{-1}) corresponding to different wind conditions in Denmark Strait (left column). The shading represents the standard error. (a) Average of all instances where the northeasterly wind in the strait is greater than the mean plus one standard deviation. (b) Instances where the wind is close to the mean. (c) Instances where the southwesterly wind is greater than the mean plus one standard deviation.

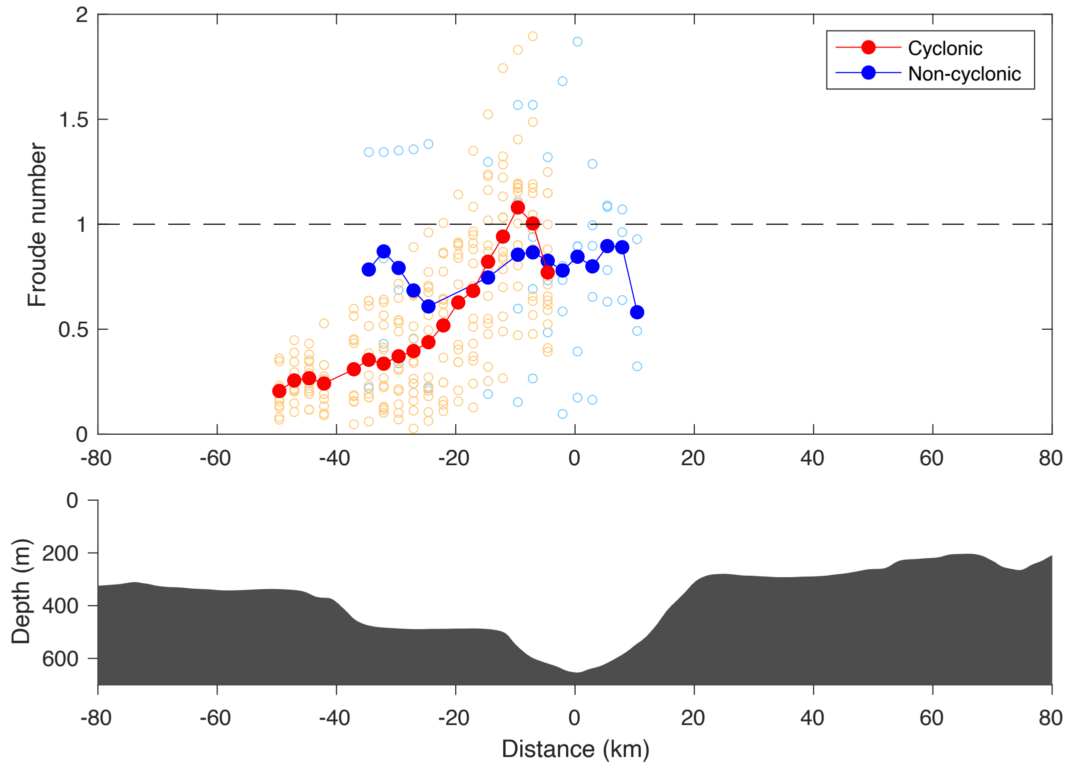

Figure 9. Composite Froude number G as a function of across-strait distance, for the cyclonic cases (red) and anti-cyclonic cases (blue). The individual values for the 22 occupations are open circles, and the mean values at each location are the filled circles. The critical value of $G = 1$ is indicated by the dashed line. The bottom panel shows the bathymetry.

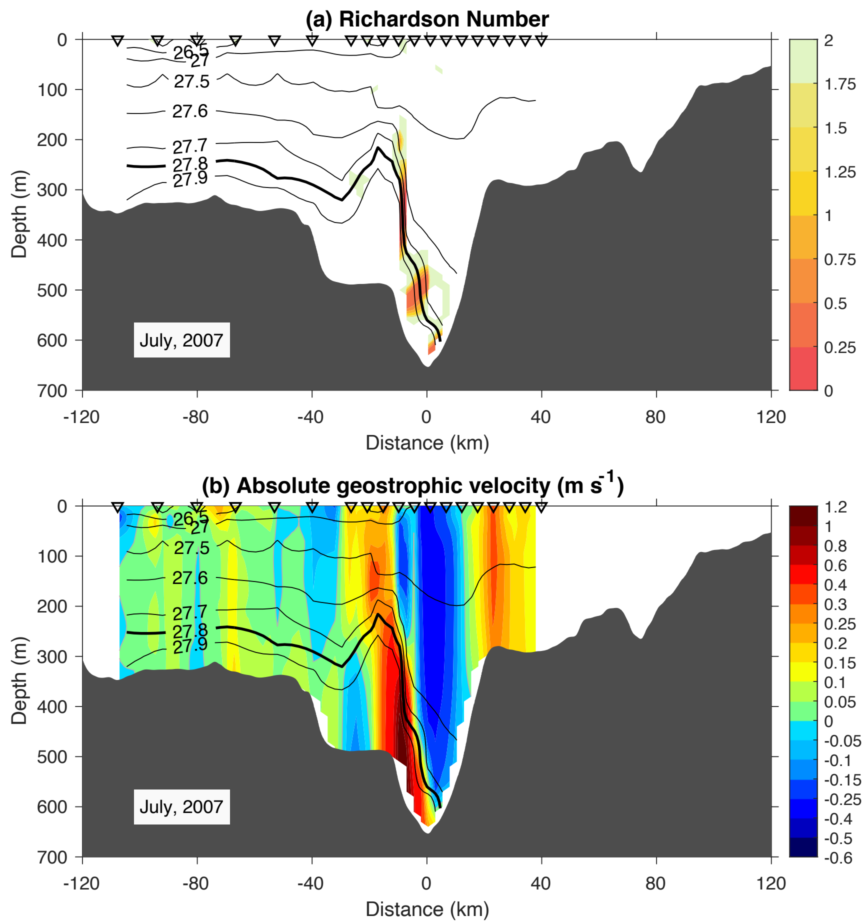

Figure 10. Vertical sections of (a) gradient Richardson number (color) and (b) absolute geostrophic velocity (m s^{-1}; color) overlain by potential density (kg m^{-3}; contours) for the Látrabjarg occupation in July, 2007. The highlighted isopycnal of 27.8 kg m^{-3} is the upper boundary of the overflow water. The inverted triangles indicate the station locations.

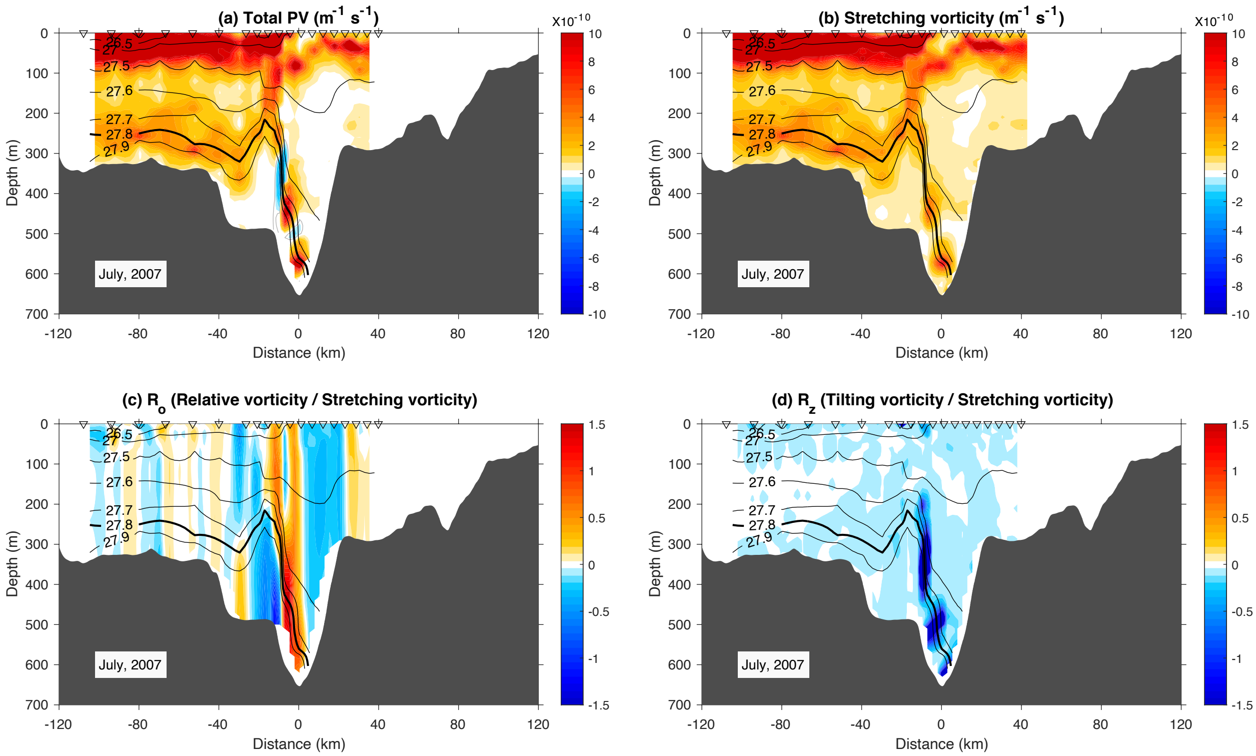

Figure 11. Vertical sections of the components of the Ertel potential vorticity (color) for the July 2007 Látrabjarg occupation, overlain by potential density (kg m^{-3}; contours). (a) Total potential vorticity (m^{-1} s^{-1} $\times$ 10^{-10}). (b) Stretching vorticity (m^{-1} s^{-1} $\times$ 10^{-10}). (c) The ratio of relative vorticity to stretching vorticity (R_o). (d) The ratio of tilting vorticity to stretching vorticity (R_z). The highlighted isopycnal of 27.8 kg m^{-3} is the upper boundary of the overflow water. The inverted triangles indicate the station locations.

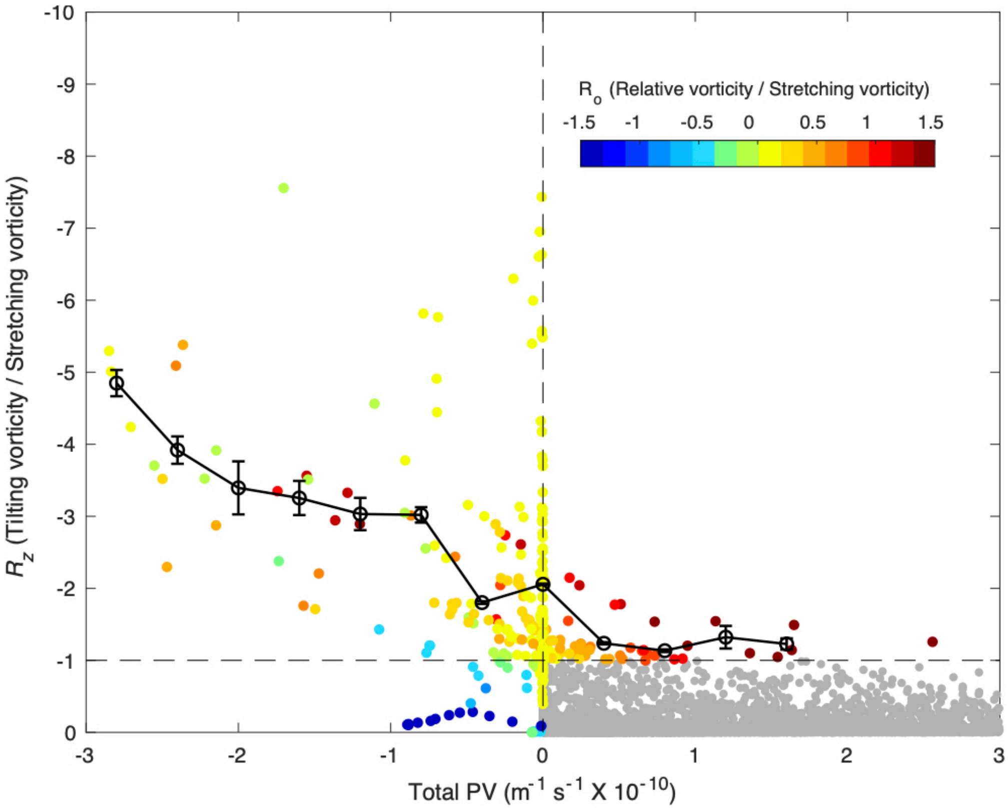

Figure 12. Scatter plot of the shear Rossby number R_z versus total the potential vorticity Π, using the 22 Látrabjarg sections with velocity. The data points are colored by the value of the Rossby number R_o except for cases when R_z > -1 and Π> 0, which are shaded grey. The black line with open circles is the average value of R_z when it is less than -1, for each PV bin (bin size of 0.4 m^{-1} s^{-1} × 10^{-10}). The standard errors are included.

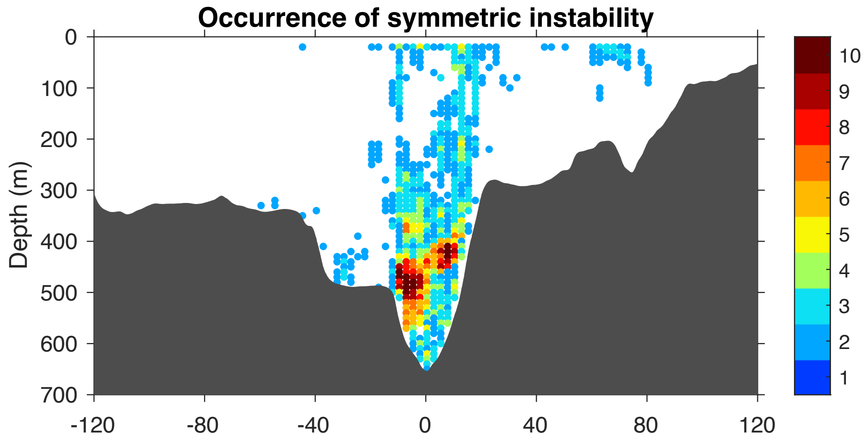

Figure 13. Occurrence of symmetric instability for the 122 hydrographic Látrabjarg sections, colored by number of realizations.

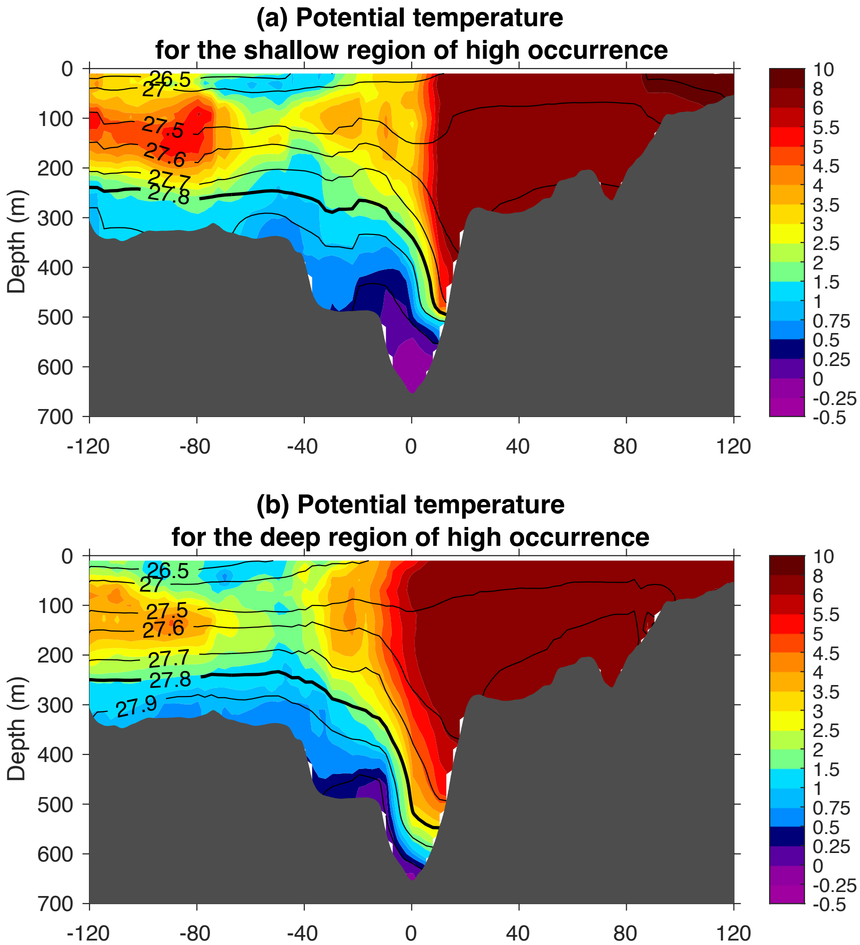

Figure 14. Composite average sections of potential temperature (°C, color) overlain by potential density (kg m^{-3}, contours) corresponding to the (a) shallow and (b) deep regions of high occurrence of symmetric instability in Fig. 13. The highlighted isopycnal of 27.8 kg m^{-3} is the upper boundary of the overflow water.